

Tuning the electronic and optical properties of $hg - C_3N_4$ quantum dots with edge-functionalization: A computational perspective

Khushboo Dange, Vaishali Roondhe, and Alok Shukla

*Department of Physics, Indian Institute of Technology Bombay, Powai, Mumbai 400076, India**

In this work, we have systematically investigated the structural, electronic, vibrational and optical properties of the edge-functionalized hg- C_3N_4 quantum dots with the aim of exploring their possible applications in solar cells and other optoelectronic devices such as light-emitting diodes. The functional groups considered in this work are methyl ($-CH_3$), fluorine ($-F$), and oxygenated groups such as aldehyde ($-CHO$), carboxyl ($-COOH$), ketone ($-COCH_3$), and hydroxyl ($-OH$) groups. The edge-functionalization resulted in significant tuning of the electronic, vibrational, and optical properties. Thus, their structural fingerprints are present in both their vibrational and optical properties, thereby allowing their detection both in the Raman as well as optical spectroscopies. It is observed that edge functionalization broadens the energy range of optical absorption, leading to coverage of most of the ultraviolet and visible regions. This implies that the edge-functionalization of hg- C_3N_4 quantum dots can be used in a variety of optoelectronic devices such as solar cells and light emitting diodes.

Keywords: hg- C_3N_4 quantum dots; density functional theory; edge-functionalization; UV-vis absorption spectra

I. INTRODUCTION

Two-dimensional (2D) materials have attracted a lot of attention from the research community since the successful exfoliation of graphene [1, 2]. Also, the synthesis of other 2D materials such as silicene [3], phosphorene [4], boron nitride [5], carbon nitride [6], silicon carbide [7], etc., has opened a novel field of research in materials with useful and promising applications in nanotechnology [8–10]. Among these, π -conjugated 2D materials are of par-

* khushboodange@gmail.com, oshivaishali@gmail.com, shukla@iitb.ac.in

ticular interest because of their unique properties which make them better candidates for multiple applications such as sensors, energy storage, electronic devices, etc. [11–17]. One such material is graphitic carbon nitride (g-C₃N₄) with a delocalized π -conjugated structure, with weak interlayer van der Waal interactions, and strong covalent intralayer bonds [18], similar to graphene. Among all carbon nitride structures, g-C₃N₄ is the most stable allotrope as compared to its other phases such as the cubic, semi-cubic, α , and β phases [19]. Furthermore, it possesses the smallest band gap as compared to its other allotropes [20]. The heptazine phase has an indirect band gap of 2.7 eV, while triazine phase possess a direct band gap of 2.9 eV [21, 22]. Additionally, an atomically thin infinite 2D monolayer of g-C₃N₄ also exists [6], and its band gap computed using the first-principles density functional theory (DFT) is reported to be 2.1 eV [23]. This material has gained widespread attention because of several reasons such as its direct band gap in the visible region, low cost, earth abundance, easy synthesis, metal-free nature, physiochemical stability, and good thermal stability [24]. 2D g-C₃N₄ covers a wide range of possible applications including photocatalytic properties both for the hydrogen evolution reaction (HER) as well as oxygen evolution reaction (OER), bioimaging, and in photoelectronic devices [16, 24–27]. In spite of all these fascinating properties, pure g-C₃N₄ has its own limitations as a photocatalytic material, low electrical conductivity, and inefficient utilization of solar energy due to its wide band gap, thereby restricting its applicability [16, 25, 27]. Patnaik et al. [28] recently reviewed the advances in designing Ag modified g-C₃N₄ based nanocomposites to enhance its photocatalytic activity. Tian et al. [29] synthesized a g-C₃N₄-BiVO₄ heterojunction which delivers high photocatalytic performance. Chemical functionalization such as carboxylation, sulfonation, amidation, and phosphorylation as well as substitutional doping with B, C, N, S, and O resulted in significant modifications of the electronic and optical properties of g-C₃N₄ [30–32]. g-C₃N₄ has been widely used in dye-sensitized solar cells (DSSC) as a photoanode to act as blocking layer to prevent charge recombination leading to improved efficiency ranging from 2.01–8.07 % [33]. It has also been added in various perovskite solar cells with the purpose of improving the coupling between the perovskite layer and the hole transport material leading to increased efficiency in the range 12.85 – 20.3 % [33].

Nowadays, research in the field of quantum dots (QDs) has received extra attention as confinement in all dimensions (0D materials) leads to effective tuning of electronic, optical, physical, and chemical properties [18, 34, 35]. Therefore, quantum confinement by con-

structuring finite structures, i.e., quantum dots of 2D g-C₃N₄ may provide us with an effective way of tuning its material properties. Since the g-C₃N₄ sheet is a periodic arrangement of two different types of unit cells, i.e., s-triazine and tri-s-triazine (also known as heptazine) [31], we can obtain two types of quantum dots from it [36]. Tri-s-triazine, as the name suggests, consists of three s-triazine rings [37], and it is attractive from the point-of-view of doping, adsorption, and tunable optoelectronic properties because extra nitrogen atoms contribute more lone pairs as compared to s-triazine-based QDs [38]. Ghashghaee et al. [39] compared the geometric structure and electronic properties of heptazine-based g-C₃N₄ (hg-C₃N₄) QDs and 2D g-C₃N₄. Olademehin et al. [40] reported the electronic and optical properties of triangular shaped g-C₃N₄ QDs of increasing sizes, designed using melamine (triazine) and heptazine units. Their study also demonstrated that the carbon and nitrogen sites would be more favorable for HER and OER, respectively. Also, the computational approach of Ullah et al. [41] gave an in-depth explanation of the better spatial confinement of frontier orbitals and charge transfer in CNQDs than in GQDs, leading to their enhanced photocatalytic activity. Their investigations were also based on the triangular QDs and reported that tuning of the optical absorption and emission depends mostly on the size, and not on the shape. Though pure g-C₃N₄ QDs are found to be promising for solar cell devices and photocatalytic activity, but their wide band gap limits their energy harvesting efficiency. Both theoretical and experimental studies have shown that the HOMO-LUMO gap of g-C₃N₄ QDs can be tuned by doping with non-metal atoms [36, 42, 43]. Zhai et al. [44] have performed a DFT-based computational study of pristine g-C₃N₄ QDs with the aim of understanding the evolution of their electronic structure and optical properties as functions of shapes and sizes. Their studies revealed that triangular lamellar structures are more suitable candidates for superior photophysical/optical properties, however, they did not consider functionalization. Bandhopadhyay et al. [43] have examined the effect of functionalization on the heterostructures composed of g-C₃N₄ QDs stacked with graphene QD, with a single electron acceptor (carboxyl) or electron donor (amine and hydroxyl) group. Functionalization of g-C₃N₄ QDs with the carboxyl (-COOH) and hydroxyl (-OH) groups has already been achieved experimentally, and tunable emission properties were obtained [45, 46]. To the best of our knowledge, no theoretical study has been reported that shows the effect of functionalization on g-C₃N₄ QDs with different electron acceptor and electron donor groups. Also, it is reported that the synthesis of g-C₃N₄ QDs leads to a high percent-

age of amine edges as well as oxygenated groups which get introduced inevitably [46]. Thus, it is important to study the effect of such functional groups on the structural, electronic, and optical properties of g-C₃N₄ QDs. In the present work, the smallest unit of heptazine and triangular shaped hg-C₃N₄ QDs comprising of three to six heptazine units are considered to investigate the effect of chemical functionalization on them. The functional groups considered in the present work include methyl (-CH₃), fluorine (-F), and oxygenated groups such as aldehyde (-CHO), carboxyl (-COOH), ketone (-COCH₃) and hydroxyl (-OH) groups. The motivation for this study comes from the work of Yunhai and collaborators on the edge-functionalized GQDs [47]. Their study revealed that the functional groups containing C=O double bond are comparatively more effective in tuning the electronic and optical properties of GQDs.

The remainder of this article is organized as follows. In the next section, we address our computational methodology in brief, followed by a detailed discussion of our results in section III. Finally, we conclude our work in section IV by summarizing the key findings.

II. COMPUTATIONAL DETAILS

All the calculations presented in this work were performed within the framework of density functional theory (DFT) [48, 49] as implemented in the Gaussian16 package [50]. The B3LYP hybrid functional [51] was employed to account for the exchange and correlation effects, coupled with the Gaussian-type valence triple zeta 6-311G [52] basis set containing two polarization functions (d, p). Some of the electronic and optical properties calculations were also performed using the HSE06 functional for comparative study. The convergence criteria was set to 10^{-8} Hartree to solve the Kohn-Sham equations [49] self-consistently. The geometry optimization iterations of all the considered structures were carried out until the gradient forces on each constituent atoms reached a minimum value of 4.5×10^{-4} Hartree/Bohr. In addition, the RMS force, maximum displacement, and RMS displacement conditions were set at 3.0×10^{-4} Hartree/Bohr, 1.8×10^{-3} Bohr, and 1.2×10^{-3} Bohr, respectively. The vibrational frequencies were also calculated to ensure the stability of the optimized structures and for none of the considered structures any imaginary frequencies were found. GaussView6 software [53] was employed for the visualization of the optimized structures and their frontier molecular orbitals (MOs) such as the HOMO and LUMO. The

partial and total density of states were generated using the Multiwfn software [54]. After the study of the electronic properties, optical properties were investigated using the time-dependent density functional theory (TD-DFT) as developed by Runge and Gross [55, 56]. The IEFPCM model [57] was used for the calculation of UV-visible absorption spectra [58].

III. RESULTS AND DISCUSSION

A. Structural and Vibrational Properties

Optimized geometries

The optimized geometries of all the considered pristine hg-C₃N₄ QDs are shown in Fig. 1. The different functionalized single heptazine units appear to remain planar (Fig. 1(a)). The calculated C–N bond lengths are in the range 1.32–1.35 Å, consistent with the previously reported work [44]. We note that with the increase in size of the hg-C₃N₄ QDs, optimized structures no longer remain planar and instead acquire buckled geometries. The reason for buckling can be related to the deformation of C–N bonds due to repulsive interactions between lone pairs present on the nitrogen atoms [44]. As the size of the hg-C₃N₄ QDs increases, the number of nitrogen atoms and the corresponding lone pairs present in the structure increases, which results in an increased order of buckling with the size of the hg-C₃N₄ QDs. The lateral sizes of all the optimized QDs are indicated in Fig. 1, and their values are presented in Table I. The calculated size of the single heptazine unit is 0.69 nm, consistent with the previously reported value [44]. Interestingly, our calculated sizes of the QDs comprising 4–6 units of heptazine are well within the reported experimental values [45, 46]. The QDs are relaxed again after attaching each of the functional groups by replacing a hydrogen atom from an edge of their optimized structures. The qualitative behavior of the optimized geometries of all the considered edge-functionalized hg-C₃N₄ QDs resembles their pristine counterpart, therefore they are shown in the same figure with one hydrogen atom being replaced by X in Fig. 1. For convenience, the notation “n–X” is used to represent the studied edge-functionalized hg-C₃N₄ QDs throughout the paper, where n denotes the number of heptazine units present in the structure, and X represents the attached functional groups, i.e., —CH₃, —CHO, —COCH₃, —COOH, —OH, —F, and Pris (pristine structure).

The detailed analysis of the optimized structures suggests that all the carbon and nitrogen atoms present in all the pristine structures are largely sp^2 hybridized, in spite of buckling. In the functionalized cases, the carbon atom of oxygenated groups that contains a carbon–oxygen double bond ($-\text{CHO}$, $-\text{COCH}_3$, $-\text{COOH}$) and is attached to the nitrogen atom of the pristine QD moieties becomes sp^2 hybridized. Whereas, the carbon, oxygen, and fluorine atoms of $-\text{CH}_3$, $-\text{OH}$, and $-\text{F}$ groups, respectively, become sp^3 hybridized while forming a bond with a nitrogen atom of the pristine structures. Table S1 of the supporting information (SI) presents the calculated bond lengths and bond angles for atoms that are near the attached functional groups. The changes in the C–N bond lengths for all the functionalized hg- C_3N_4 QDs are in the range 0.02–0.05 Å, with the maximum bond lengths for the oxygenated groups (1.38 Å) and the fluorine group (1.39 Å). The reason for such small distortions in bond length is that only a single functional group is attached at the edge of hg- C_3N_4 QDs. Due to such small distortions, the contribution of structural influences on the electronic and optical properties of edge-functionalized hg- C_3N_4 QDs should be minimal.

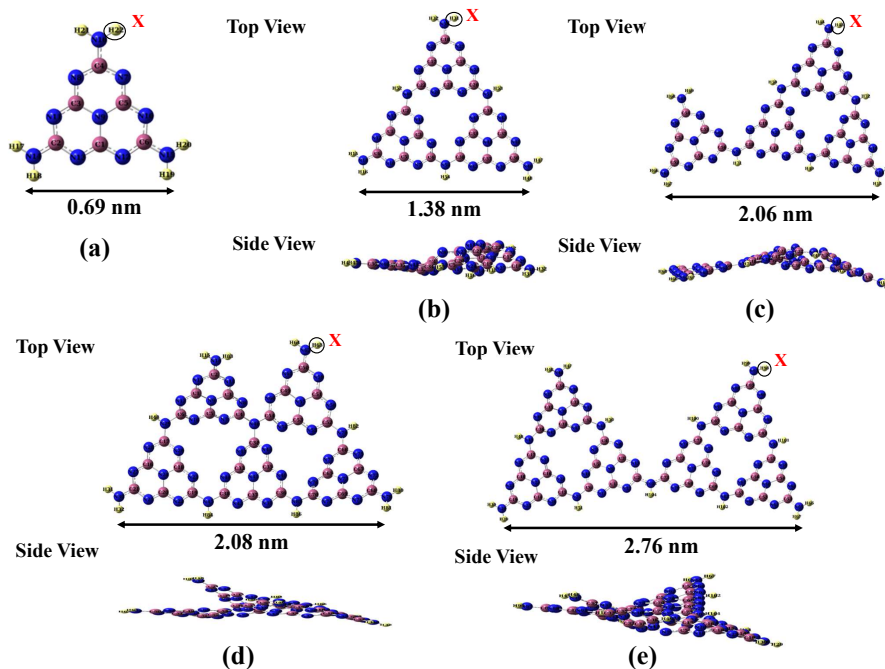


Figure 1. Optimized structures of (a) 1-X, (b) 3-X, (c) 4-X, (d) 5-X, and (e) 6-X hg - C_3N_4 quantum dots. Blue, pink, and yellow spheres represent the nitrogen, carbon, and hydrogen atoms, respectively, while X denotes the attached functional groups ($-CH_3$, $-CHO$, $-COCH_3$, $-COOH$, $-OH$, and $-F$). Lateral size of each QD is indicated by a double-arrow line.

Vibrational Properties

In order to confirm the stability of the optimized structures, vibrational frequency calculations are performed. Total $3n - 6$ vibrational modes are obtained for each structure, where n represents the total number of atoms present in that structure. The lack of imaginary frequencies confirms that the structural minima are likely to have been obtained. For all the structures considered, the minimum vibrational frequencies are reported in Table I, which in all the cases correspond to an out-of-plane vibrational mode. For further investigation of the vibrational properties, we have also calculated the corresponding Raman spectra, presented in Fig. S1 of the SI. A brief description related to some of the unique vibrational modes is also included in SI.

Table I. Lateral size (L) and minimum vibrational frequencies (Freq) for all the considered structures, including the pristine one (-Pris).

Structure	L (nm)	Freq (cm ⁻¹)	Structure	L(nm)	Freq (cm ⁻¹)
1 - <i>Pris</i>	0.69	95	4 - <i>COOH</i>	2.06	4.01
1 - <i>CH₃</i>	0.69	55.03	4 - <i>OH</i>	2.06	6.79
1 - <i>CHO</i>	0.69	40.24	4 - <i>F</i>	2.06	6.81
1 - <i>COCH₃</i>	0.69	33.30	5 - <i>Pris</i>	2.08	10.09
1 - <i>COOH</i>	0.69	37.11	5 - <i>CH₃</i>	2.08	9.72
1 - <i>OH</i>	0.69	74.98	5 - <i>CHO</i>	2.08	10.15
1 - <i>F</i>	0.69	72.30	5 - <i>COCH₃</i>	2.08	10.08
3 - <i>Pris</i>	1.38	24.5	5 - <i>COOH</i>	2.08	10.10
3 - <i>CH₃</i>	1.38	22.07	5 - <i>OH</i>	2.08	9.96
3 - <i>CHO</i>	1.38	19.20	5 - <i>F</i>	2.08	10.14
3 - <i>COCH₃</i>	1.38	16.71	6 - <i>Pris</i>	2.76	3.62
3 - <i>COOH</i>	1.38	17.24	6 - <i>CH₃</i>	2.76	3.83
3 - <i>OH</i>	1.38	22.13	6 - <i>CHO</i>	2.76	3.94
3 - <i>F</i>	1.38	21.85	6 - <i>COCH₃</i>	2.76	4.14
4 - <i>Pris</i>	2.06	7.81	6 - <i>COOH</i>	2.76	4.07
4 - <i>CH₃</i>	2.06	6.80	6 - <i>OH</i>	2.76	3.81
4 - <i>CHO</i>	2.06	5.20	6 - <i>F</i>	2.76	3.87
4 - <i>COCH₃</i>	2.06	4.57			

B. Electronic Properties

After confirming the stability of the edge-functionalized hg-C₃N₄ QDs, next, we investigate their electronic properties using B3LYP functional. In Table II and Table III we present highest occupied molecular orbital (HOMO) energy E_{HOMO} , the lowest unoccupied molecular orbital (LUMO) energy E_{LUMO} , the HOMO-LUMO energy gap (E_g), and the charge transfer.

We note that E_g for the pristine hg-C₃N₄ QDs decreases with the increasing size from 4.99

eV to 2.83 eV, clearly due to quantum confinement. The modification in E_g for the different sizes is related to the variation of E_{HOMO} and E_{LUMO} values with the increasing size of the QD. The HOMO and LUMO levels represent the electron donor (nucleophilic) and electron acceptor (electrophilic) properties of the system, respectively. As the sizes of the pristine QDs increase, LUMO energy levels get lowered continuously as is clear from the values presented in Table II and Table III, while for E_{HOMO} values, non-monotonic decrease is observed.

After the pristine structures, next we discuss the electronic properties of the functionalized QDs. From Table II and Table III it is obvious that edge-functionalization causes significant changes in the values of HOMO/LUMO energies and consequently in the HOMO-LUMO gaps of the QDs. It is observed that for all the edge-functionalized hg-C₃N₄ QDs (except 6 - X QDs), the E_{HOMO} values of those functionalized with the $-CH_3$ group increase with respect to their pristine counterparts, which implies increment in their electron-donor ability. However, functionalization with other groups leads to reduced E_{HOMO} values, indicating reduced electron-donor abilities of the corresponding QDs. Similarly, E_{LUMO} values of the QDs functionalized with the $-CH_3$ are seen to increase with respect to the pristine QDs, suggesting their reduced electron-acceptor ability. However, in the case of other functional groups, E_{LUMO} values are seen to decrease with respect to the corresponding pristine QDs implying increased electron-acceptor ability. For the case of 6 - X QDs, we observe a different behavior; E_{HOMO} values get lowered and E_{LUMO} values are increased for all the groups compared to their pristine counterparts. Thus, the uneven shifting of the HOMO and LUMO levels resulted in the tuning of E_g which depends on the following two factors: (a) frontier orbital interaction (FOI), and (b) charge transfer. According to frontier molecular orbital (FMO) theory [59, 60], interaction between frontier orbitals (HOMO and LUMO) leads to hybridization and reduces the energy gap between them. However, charge transfer from the QD moiety to the attached functional group leads to a reduction in the screening of electrons. The enhancement of electronic screening with the increase in electron density and vice versa has already been reported previously in the literature [61, 62]. The reduction in electronic screening will increase the electron-electron interaction, which in turn increases the energy gap. Therefore, the tuned E_g depends on the competition between FOI and the charge transfer [47].

We have performed the Mulliken charge analysis and then calculated the amount of charge

transfer from the hg-C₃N₄ QD moiety to the attached functional group or vice-versa. The calculated charge transfers for all the pristine and functionalized structures are presented in Table II and Table III. We note that for the pristine QDs, the charge transfer is between the QD moiety and that H-atom which is replaced by a functional group in the case of functionalized QDs. If the charge is transferred from the QD moiety to the attached functional group or the H atom, i.e., there is an electron transfer from the H atom or the functional group to the QD moiety, the charge transfer is assigned a positive sign. However, if there is a net electron transfer in the opposite direction, i.e., from the QD moiety to the H atom or the functional group, the charge transfer is assigned a negative sign. We note that the charge transfer as defined above is positive in all the cases except for the functional groups $-OH$ and $-F$, for which it is negative. The $-OH$ and $-F$ groups because of their high electronegativities gain electrons from the QD moiety, which justifies their electron withdrawing nature, also reported for the GQDs edge-functionalized with these two groups [47]. Also, the amount of electron transfer to the $-OH$ group is less than that to the $-F$ group because comparatively speaking $-F$ group is more electronegative than the $-OH$ group. Further, the positive value of charge transfer in the case of $-CH_3$ group is in accordance with its electron donating nature, reported for the $-CH_3$ functionalized GQDs also [47]. The amount of charge transfer reveals the extent to which E_g increases. Considering the case of 6- CHO and 6- $COCH_3$, charge transfer is more in case of $-CHO$ group, which leads to a large E_g . As stated earlier, the effects of structural distortions are minimal in this work; the increment or decrement of E_g is induced by the FOI and charge transfer. The resultant E_g for 1- CH_3 QD gets increased as compared to its pristine counterpart, while it gets lowered in the case of other 1- X structures. The opposite trend is noticed in 5- X QDs, as E_g is reduced only for 5- CH_3 QD. In cases of 3- X and 4- X QDs, E_g is reduced compared to their pristine counterparts, except for $-OH$ functionalized cases. Also, for 3- CH_3 QD, no change is noticed, which implies that the effective contribution of charge transfer and FOI after functionalization is equal, and thus the cancellation of their effects takes place. In case of 6- X QDs, edge-functionalization resulted in increased E_g for all the considered functional groups. The reason for larger E_g than their pristine counterpart in some of the cases implies that the influence of the charge transfer is greater than the effect of FOI. However, reduced E_g in other cases reveals that the effective contribution of FOI and charge transfer is such that the FOI dominates.

Furthermore, we have also calculated E_{HOMO} , E_{LUMO} , and E_g values using the HSE06 functional (Tables II and III) for comparison. In this case also, uneven shifting of E_{HOMO} and E_{LUMO} values is observed as depicted in Tables II and III. Compared to the B3LYP results, the HSE06 functional based E_g values are lower for all the considered structures. The E_g obtained for 1-Pris (4.67 eV) and 3-Pris (3.55 eV) QDs using HSE06 functional are relatively closer to the values reported in the literature [40]. The trends observed in the shifting of the HOMO and LUMO levels for the pristine and corresponding functionalized cases are similar to those of the B3LYP based results.

Table II. Calculated energies of the HOMO (E_{HOMO}), LUMO (E_{LUMO}), energy gap (E_g), and the charge transfer from the QD moiety to the attached functional group or vice-versa for 1- X , 3- X , and 4- X structures. *Pris* indicates the pristine QD, without any attached functional group.

Structures	E_{HOMO} (eV)		E_{LUMO} (eV)		E_g (eV)		Charge Transfer (e)
	B3LYP	HSE06	B3LYP	HSE06	B3LYP	HSE06	B3LYP
1- <i>Pris</i>	-6.25	-6.11	-1.26	-1.47	4.99	4.67	0.25
1- CH_3	-6.20	-6.23	-1.19	-1.40	5.01	4.83	0.17
1- CHO	-6.56	-6.42	-1.91	-2.12	4.65	4.30	0.02
1- $COCH_3$	-6.46	-6.32	-1.76	-1.97	4.70	4.35	0.07
1- $COOH$	-6.52	-6.39	-1.77	-1.98	4.75	4.40	0.03
1- OH	-6.36	-6.37	-1.48	-1.48	4.88	4.89	-0.01
1- F	-6.61	-6.47	-1.79	-2.00	4.82	4.47	-0.19
3- <i>Pris</i>	-6.31	-6.19	-2.40	-2.64	3.91	3.55	0.23
3- CH_3	-6.28	-6.15	-2.37	-2.60	3.91	3.55	0.20
3- CHO	-6.46	-6.34	-2.65	-2.89	3.81	3.45	0.06
3- $COCH_3$	-6.41	-6.29	-2.57	-2.80	3.84	3.48	0.09
3- $COOH$	-6.44	-6.32	-2.60	-2.84	3.84	3.48	0.04
3- OH	-6.41	-6.29	-2.49	-2.72	3.92	3.57	-0.01
3- F	-6.49	-6.37	-2.64	-2.87	3.85	3.49	-0.16
4- <i>Pris</i>	-6.36	-6.24	-2.56	-2.80	3.80	3.44	0.23
4- CH_3	-6.32	-6.21	-2.53	-2.77	3.79	3.44	0.22
4- CHO	-6.50	-6.38	-2.76	-3.00	3.74	3.38	0.11
4- $COCH_3$	-6.45	-6.33	-2.70	-2.93	3.75	3.40	0.13
4- $COOH$	-6.48	-6.36	-2.72	-2.96	3.76	3.41	0.09
4- OH	-6.45	-6.33	-2.63	-2.87	3.82	3.46	-0.01
4- F	-6.52	-6.40	-2.75	-2.99	3.76	3.41	-0.14

Table III. Calculated energies of the HOMO (E_{HOMO}), LUMO (E_{LUMO}), energy gap (E_g), and the charge transfer from the QD moiety to the attached functional group or vice-versa for 5 – X and 6 – X structures. *Pris* indicates the pristine QD, without any attached functional group.

Structures	E_{HOMO} (eV)		E_{LUMO} (eV)		E_g (eV)		Charge Transfer (e)
	B3LYP	HSE06	B3LYP	HSE06	B3LYP	HSE06	
5 – <i>Pris</i>	-6.28	-6.16	-2.76	-3.01	3.52	3.15	0.28
5 – CH_3	-6.25	-6.13	-2.75	-2.99	3.50	3.14	0.21
5 – CHO	-6.44	-6.32	-2.88	-3.12	3.56	3.20	0.05
5 – $COCH_3$	-6.39	-6.27	-2.84	-3.09	3.55	3.18	0.09
5 – $COOH$	-6.41	-6.30	-2.85	-3.10	3.56	3.20	0.04
5 – OH	-6.38	-6.27	-2.82	-3.07	3.56	3.20	-0.01
5 – F	-6.46	-6.34	-2.88	-3.13	3.58	3.22	-0.14
6 – <i>Pris</i>	-6.33	-5.91	-3.50	-3.53	2.83	2.38	0.28
6 – CH_3	-6.38	-6.26	-2.77	-3.01	3.61	3.25	0.24
6 – CHO	-6.45	-6.34	-2.90	-3.14	3.55	3.19	0.11
6 – $COCH_3$	-6.44	-6.33	-2.86	-3.10	3.58	3.22	0.15
6 – $COOH$	-6.45	-6.33	-2.88	-3.02	3.57	3.21	0.09
6 – OH	-6.43	-6.32	-2.84	-3.08	3.59	3.23	-0.01
6 – F	-6.45	-6.33	-2.90	-3.15	3.55	3.19	-0.13

To further investigate the electronic properties, both the total density of states (TDOS) and partial density of states (PDOS) are calculated for each of the edge-functionalized $hg-C_3N_4$ QDs using the B3LYP functional, and the results are plotted in Fig. 2 for the 3– X QDs, and in Figs. S2—S5 of the SI for 1– X , 4– X , 5– X , and 6– X QDs, respectively. As shown in Fig. 2, the TDOS plots for 3– X QDs have two common features, i.e., (a) there are five peaks visible in the occupied-orbital region, and (b) the three peaks (the highest one is hidden in the green region) in the unoccupied-orbital region. As is obvious from Figs. S3—S5 of the SI, that the similar trends in TDOS are obtained for 4– X , 5– X , and 6– X QDs also. However, for 1– X QDs a shoulder peak corresponding to the third peak of the occupied region is clearly visible as depicted in Fig. S2 of the SI. The PDOS provides the contribution of each constituent

atom individually to the TDOS. It is clear from Fig. 2 that in the case of $3 - X$ QDs, in the occupied region, the maximum contribution to TDOS is from the hydrogen atoms, followed by nitrogen and carbon atoms whereas in the unoccupied region, nitrogen atoms contribute the most for all the QDs, while H atoms make the next most important contributions for $3 - \text{Pris}$ and $3 - \text{CH}_3$. For the QDs functionalized with the O-based groups or F atom, O and F atoms also contribute significantly to the TDOS in the unoccupied region for the $3 - X$ QDs (see Figs. 2(c)—(g)). Similar behavior of PDOS is obtained for $4 - X$, $5 - X$, and $6 - X$ QDs, presented in Fig. S3–S5 of the SI, respectively. In the case of $1 - X$ QDs (Fig. S2 of the SI), in addition to the above behavior, a minor contribution of carbon atoms (hidden in the magenta region in the case of oxygenated and fluorinated groups) is also present in the unoccupied region, which is missing in other structures. It is also noted that both the TDOS and PDOS plots are quite similar for the pristine and corresponding functionalized structures, which indicates that the edge-functionalization of $hg - C_3N_4$ QDs with a single functional group has a minimal influence on the electronic structure of $hg - C_3N_4$ QDs. The isosurfaces of the HOMO and LUMO corresponding to $3 - X$ structures are depicted in the insets of Figs. 2, and corresponding to $1 - X$, $4 - X$, $5 - X$, and $6 - X$ structures are illustrated in the inset of Figs. S2—S5 of the SI, respectively. For the single heptazine unit ($1 - \text{Pris}$) structure [Fig. S2(a) of the SI], it is clear that the HOMO is localized on the nitrogen atoms, whereas the LUMO is delocalized and mainly distributed over the C–N bonds and located on the nitrogen atoms present at the boundary, in agreement with the literature [40, 44]. After functionalization of $1 - \text{Pris}$ QD, the type of spatial distribution of both the HOMO (localized) and LUMO (delocalized) remains unaffected. In addition to this, LUMO also gets distributed over the atoms of the attached functional groups except in the case of $-\text{CH}_3$ group. When we examine the HOMO and LUMO plots of the larger QDs, we find that the spatial distribution of both the HOMO and LUMO shows behavior similar to that of the $1 - X$ structures. We have also plotted the isosurfaces of the HOMO and LUMO levels using the HSE06 functional for the $1 - X$ structures and shown in Fig. S6 of the SI. The spatial distribution of these orbitals is similar to that obtained using the B3LYP functional.

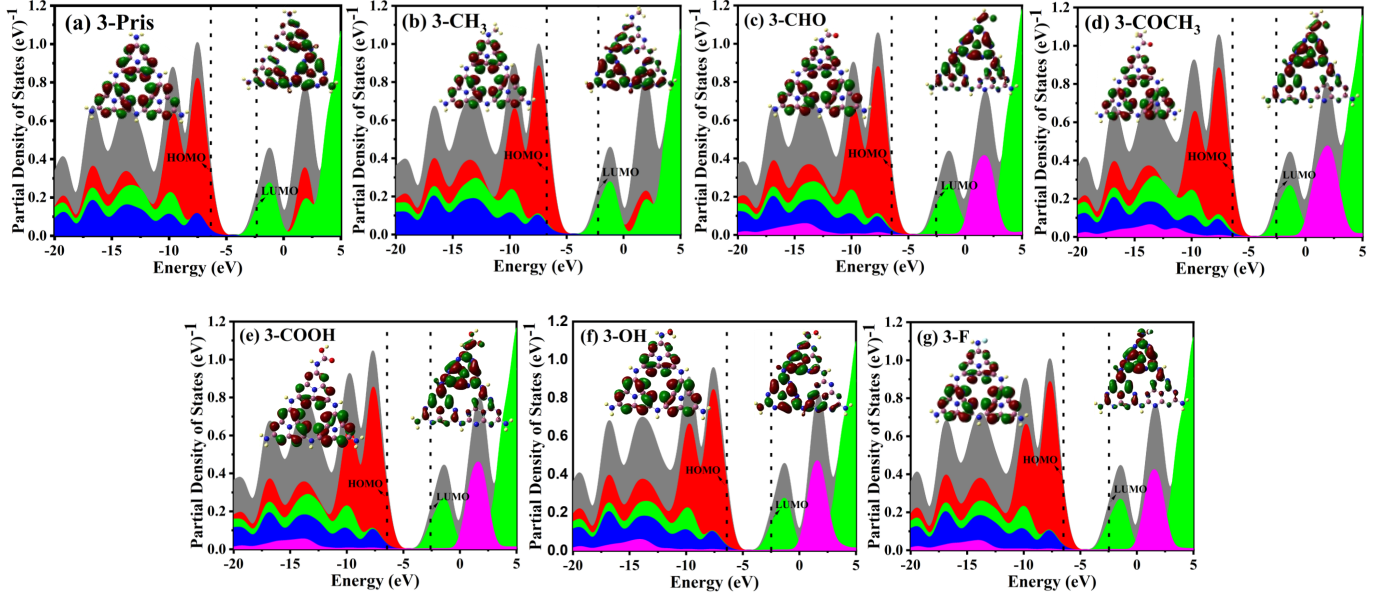


Figure 2. Total and partial density of states plots of (a) 3 – *Pris*, (b) 3 – CH_3 , (c) 3 – CHO , (d) 3 – $COCH_3$, (e) 3 – $COOH$, (f) 3 – OH , and (g) 3 – F structures. Grey color represents the TDOS. Red, green, blue, and magenta colors represent the contributions of H, N, C, and O or F atoms, respectively. The corresponding HOMO and LUMO are shown in the inset of each plot.

C. Optical Absorption Spectra

In this section we present and discuss the optical absorption spectra of the edge-functionalized $hg - C_3N_4$ QDs computed using the TD-DFT approach [55, 56] under different conditions, and compare them to those of the corresponding pristine QDs. The absorption spectra are computed for 20 excited states. First, we calculated the absorption spectra using B3LYP with water as the solvent (B3LYP+water), as these QDs are found to be soluble in water [63]. The calculated spectra of all the pristine and functionalized structures using B3LYP+water are plotted in Fig. 3, while their computed optical gaps are presented in Table IV. In addition, the calculated UV-vis absorption spectra of only the pristine $hg - C_3N_4$ QDs are separately presented in Fig. S7 of the SI.

First we note that our spectra of the pristine QDs are in good agreement with the previously reported calculations of Zhai et al. [44]. In our calculations, the strongest absorption peaks in case of 1 – *Pris* and 3 – *Pris* structures are at 205 nm (6.03 eV) and 284 nm (4.36 eV), respectively, in agreement with their results [44]. As far as the size dependence of the spectra

of the pristine QDs is concerned, we note that the absorption energy range gets extended with the increase in the size of the $hg - C_3N_4$ QDs. With the increase in the size of the QD from 1-Pris to 6-Pris, the optical gap (E_g^{op}) gets reduced from 5.10 eV to 2.44 eV, leading to significant red shift also in the corresponding absorption energy ranges. As a result, the most prominent or strongest absorption peak red shifts from 205 nm (6.03 eV) (1-Pris) to 455 nm (2.72 eV) (6-Pris). Thus, taking into account the calculated absorption spectra of all the pristine QDs (1-Pris — 6-Pris), their combined absorption range (200–550 nm or 2.25–6.20 eV) covers most of the UV-Vis region of the spectrum, and also lies within the range measured experimentally [63].

From the UV-vis absorption spectra of the edge-functionalized $hg - C_3N_4$ QDs along with their pristine counterparts (see Fig. 3), it is evident that the chemical functionalization at an edge of a given QD alters both the location as well intensity of the most intense peak. Consequently, some of the functionalized structures undergo a red shift, while some others experience a blue shift in the location of the most intense peak compared to their pristine counterpart. In addition to this, a slight variation in the total number of peaks is also observed clearly due to the emergence of new energy levels due to functionalization. However, the qualitative behavior of all the edge-functionalized $hg - C_3N_4$ QDs resembles quite well that of their pristine counterparts. In case of $-COOH$ and $-OH$ groups, our calculated absorption ranges lie within the ranges reported experimentally [45, 46]. As mentioned above, the functionalization of all the considered $hg - C_3N_4$ QDs extended the absorption range covered as compared to the pristine structures. For example, the absorption range of the 1-Pris structure 200–250 nm gets extended to 200–300 nm when functionalized with the $-OH$ group (Fig. 3(a)). Thus, by functionalizing the $hg - C_3N_4$ QDs in a controlled manner we can tune their absorption ranges to make them suitable for effective utilization of solar energy. Thus appropriately functionalized $hg-C_3N_4$ QDs can be useful in solar cells.

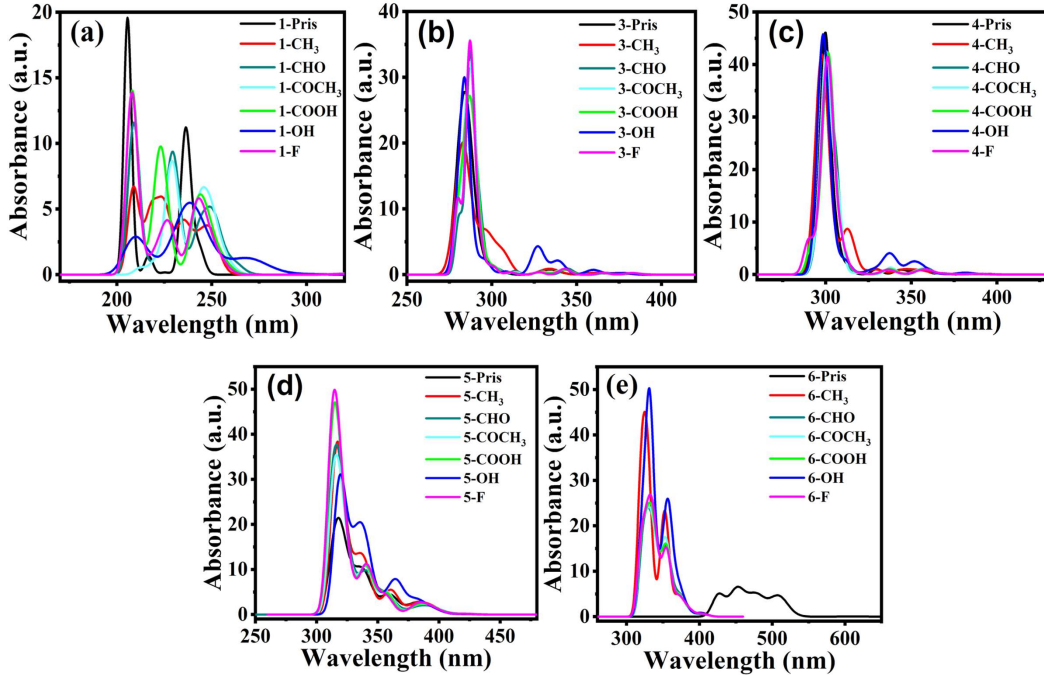


Figure 3. TD-DFT level UV-visible absorption spectra of (a) 1 – X, (b) 3 – X, (c) 4 – X, (d) 5 – X, and (e) 6 – X structures computed using B3LYP, with water as the solvent.

The optical absorption spectra are again simulated using the B3LYP functional, but this time without including any solvent (B3LYP+vacuum), i.e., in the gas phase. The resultant plots are illustrated in Fig. 4, from which it is observed that the qualitative nature of the overall spectra along with the peak positions are quite similar to that obtained using B3LYP+water condition (Fig. 3). However, compared to the B3LYP+water-based spectra, a slight reduction in the absorbance is observed for the 1-X QDs, while it is reduced significantly for other structures. Interestingly, we found that the most intense peak position corresponding to 3-Pris QD (281.64 nm) using B3LYP+vacuum is relatively close to that reported in literature [44]. In addition, the maximum absorbance peak position for 5-Pris QD (325.42 nm) also matches quite well with the literature [44]. We have also calculated the E_g^{op} corresponding to each of the edge-functionalized structures, as listed in Table IV. In the case of B3LYP+vacuum, E_g^{op} values range from 2.34 eV – 5.05 eV, and compared to the earlier results (B3LYP+water), some changes are observed. However, the total absorption

range covered by all the QDs (1-X to 6-X) in vacuum is consistent with that obtained using water as the solvent (200 nm – 550 nm).

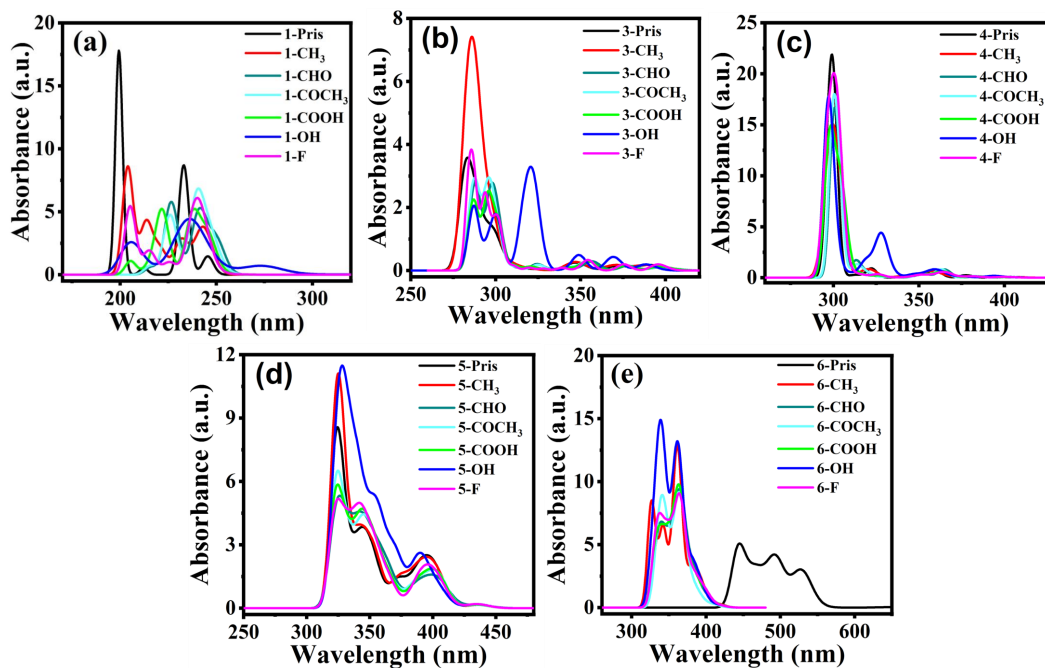


Figure 4. TD-DFT level UV-visible absorption spectra of (a) 1 – X, (b) 3 – X, (c) 4 – X, (d) 5 – X, and (e) 6 – X structures computed using B3LYP+vacuum.

Table IV. TD-DFT level optical gaps (E_g^{op}) of the considered pristine as well as functionalized hg - C_3N_4 QDs calculated using the B3LYP functional, assuming the QDs to be in vacuum, or dissolved in water. Additionally, the results obtained using the HSE06 functional, and a dielectric constant 7.5 corresponding to the g - C_3N_4 crystalline phase, are also presented.

Molecule	E_g^{op} (eV)			Molecule	E_g^{op} (eV)		
	B3LYP		HSE06		B3LYP		HSE06
	Water	Vacuum	Crystal		Water	Vacuum	Crystal
1 – <i>Pris</i>	5.10	5.05	5.20	4 – <i>COOH</i>	3.45	3.40	3.45
1 – <i>CH₃</i>	4.96	4.99	5.06	4 – <i>OH</i>	3.48	3.42	3.48
1 – <i>CHO</i>	4.74	4.96	4.86	4 – <i>F</i>	3.45	3.39	3.45
1 – <i>COCH₃</i>	4.80	4.86	4.93	5 – <i>Pris</i>	3.45	3.33	3.44
1 – <i>COOH</i>	4.84	4.89	4.96	5 – <i>CH₃</i>	3.44	3.32	3.43
1 – <i>OH</i>	4.60	4.52	4.68	5 – <i>CHO</i>	3.46	3.42	3.46
1 – <i>F</i>	4.86	4.93	4.95	5 – <i>COCH₃</i>	3.47	3.42	3.46
3 – <i>Pris</i>	3.30	3.33	3.73	5 – <i>COOH</i>	3.47	3.51	3.47
3 – <i>CH₃</i>	3.44	3.56	3.42	5 – <i>OH</i>	3.40	3.51	3.39
3 – <i>CHO</i>	3.60	3.47	3.61	5 – <i>F</i>	3.47	3.51	3.47
3 – <i>COCH₃</i>	3.62	3.49	3.64	6 – <i>Pris</i>	2.44	2.34	2.47
3 – <i>COOH</i>	3.61	3.49	3.63	6 – <i>CH₃</i>	3.34	3.26	2.47
3 – <i>OH</i>	3.35	3.36	3.50	6 – <i>CHO</i>	3.34	3.25	3.36
3 – <i>F</i>	3.60	3.50	3.63	6 – <i>COCH₃</i>	3.34	3.37	3.43
4 – <i>Pris</i>	3.48	3.44	3.49	6 – <i>COOH</i>	3.34	3.25	3.44
4 – <i>CH₃</i>	3.48	3.45	3.51	6 – <i>OH</i>	3.34	3.25	3.37
4 – <i>CHO</i>	3.45	3.39	3.44	6 – <i>F</i>	3.34	3.25	3.43
4 – <i>COCH₃</i>	3.46	3.41	3.46				

In Tables S2–S6 of the SI, we provide information related to the excited states of the considered QDs which contribute to the most intense peaks in the absorption spectra obtained using B3LYP+water. This information includes the peak locations (excitation energies), oscillator strengths (f), and the excited state wave functions. In addition, Table S7 of the SI contains the same information for the first excited state of each structure. In the TD-DFT

approach, every excited state wave function is a linear combination of several configurations each of which corresponds to a single excitation from an occupied orbital to a virtual one. The TD-DFT wave function of the first excited state of each QD (pristine or functionalized) is dominated by the configuration corresponding to the excitation of an electron from HOMO to LUMO, denoted as $H \rightarrow L$. However, f corresponding to the first excited state for all the pristine QDs is negligible, and even after functionalization exhibits no significant increase, as shown in Table S7 of the SI. Therefore, the optical gap (Table IV) is larger than the excitation energies of the first excited states for all the QDs considered in this work.

Next we consider the optical excitations of the 4- X QDs, presented in Table S4 of the SI. It is observed that the functional groups containing the $C = O$ bond and the $-F$ group resulted in the red shift of the absorption peaks, whereas the $-CH_3$ and $-OH$ groups resulted in the blue shift compared to the pristine QD. In agreement with our calculations, the red shift of the peaks is observed in the experiment performed on the QDs functionalized with the $-COOH$ group [45]. The excited state leading to the most intense peak of 4-*Pris* QD is written as 16^1A , which signifies the 16^{th} TD-DFT singlet excited state. As is obvious from the table, the wave function of this excited state derives important contributions from the configurations $H - 6 \rightarrow L + 1$, $H - 6 \rightarrow L$, and $H - 7 \rightarrow L$. The excited state corresponding to most intense peak in case of 4- CH_3 QD is 18^1A , with the wave function composed predominantly of configurations $H - 7 \rightarrow L$, $H - 8 \rightarrow L$, and $H - 5 \rightarrow L$. In a similar manner, the optical transitions corresponding to the most intense peak are presented for each of the considered pristine and edge-functionalized $hg - C_3N_4$ QD in those tables. In case of 6- X QDs (Table S6), edge-functionalization with all the considered groups resulted not only in an abrupt blue-shift of the most intense peak position, but also in the range of the absorption spectrum from the visible to the UV region after functionalization. In addition to analyzing the orbitals involved in the transitions corresponding to various absorption peaks, we have also studied the spatial distribution of electrons and holes in the first excited state, and the one giving rise to the most intense peak (the excited state with the maximum f value). For the purpose, we have used the approach of Liu et al. [64] in which the hole and electron spatial distributions are defined in terms of corresponding densities

$$\rho^{hole}(\mathbf{r}) = \sum_{i \rightarrow a} (w_i^a)^2 \phi_i(\mathbf{r}) \phi_i(\mathbf{r}) + \sum_{i \rightarrow a} \sum_{j \neq i \rightarrow a} w_i^a w_j^a \phi_i(\mathbf{r}) \phi_j(\mathbf{r}) \quad (1)$$

$$\rho^{electron}(\mathbf{r}) = \sum_{i \rightarrow a} (w_i^a)^2 \phi_a(\mathbf{r}) \phi_a(\mathbf{r}) + \sum_{i \rightarrow a} \sum_{i \rightarrow b \neq a} w_i^a w_i^b \phi_a(\mathbf{r}) \phi_b(\mathbf{r}), \quad (2)$$

where i, j and a, b are the indices denoting to the occupied (hole) and virtual (electron) MOs, respectively. The numbers w_i^a are obtained from the TD-DFT calculations, and represent the coefficients of the singly-excited configurations in which an electron is promoted from the occupied MO $\phi_i(\vec{r})$ to the virtual MO $\phi_a(\vec{r})$. We calculated the densities $\rho^{hole}(\vec{r})/\rho^{electron}(\vec{r})$ using the Multiwfn software [54], and the results are presented in Figs. S8 – Fig. S12 of the SI for all the considered edge-functionalized $hg - C_3N_4$ QDs.

After the study of optical properties using the B3LYP functional, the UV-vis optical absorption spectra were also computed using a range separated hybrid functional HSE06. These calculations were performed to explore the influence of: (a) a modern range-separated hybrid functional, and (b) crystalline environment. The crystalline form is considered because the $g - C_3N_4$ QDs also exist in the crystalline structures [65]. Therefore, during the simulation of optical absorption spectra using the HSE06 functional, a dielectric medium relevant to crystalline $hg - C_3N_4$ QDs is taken into consideration [66, 67]. For simulating the dielectric medium within the IEFPCM model, dielectric constant is taken to be 7.5 which is the value corresponding to the crystalline carbon nitrides [68]. The UV-vis optical absorption spectra computed in the crystalline environment using HSE06 functional are presented in Fig. 5. It is observed that the qualitative behavior of these spectra is similar to those simulated using B3LYP+water (Fig. 3). Except for the 5-X QDs, slight variations in the maximum absorbance values are observed. In the case of 1-X structures, chemical functionalization resulted in the red shifting of peaks corresponding to maximum absorbance compared to their pristine counterpart. However, opposite trend, i.e., blue shift is noticed after functionalization of the 6-Pris QD. Chemical functionalization of 5-Pris QD also leads to blue shift of the peaks except 5-OH structure for which red shift is observed. In the case of 3-X and 4-X QDs, except $-CH_3$, all other functional groups lead to a red shift of the most intense peak. Furthermore, again the complete absorption range covered (200 nm – 550 nm) is same as that obtained using the B3LYP functional both with water and vacuum. Next, the E_g^{op} values are also calculated for the HSE06+crystal condition, and the values are reported in Table IV. It is to be noticed that for most of the structures $(E_g^{op})_{HSE06+crystal} > (E_g^{op})_{B3LYP+water}$, while the opposite results are obtained for some of the structures.

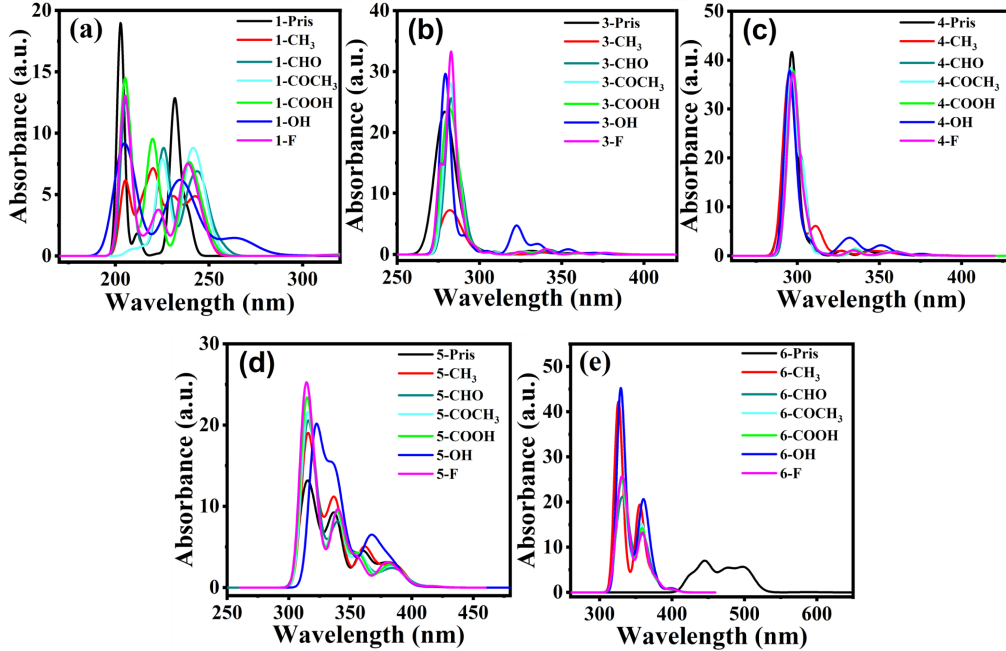


Figure 5. TD-DFT level UV-visible absorption spectra of (a) 1 – X, (b) 3 – X, (c) 4 – X, (d) 5 – X, and (e) 6 – X structures computed using the HSE06 functional and a crystalline environment.

After the calculation of optical properties using three different conditions, we tried to compare our obtained E_g^{op} values with some experimental results. The two different studies reported that the peaks in the photoluminescence spectra of $hg - C_3N_4$ QDs lie at 367 nm (3.39 eV)[46] and 467 nm (2.65 eV) [45]. The size distribution of their $hg - C_3N_4$ QDs is within the range of 2 nm - 4 nm. Compared to these experimental findings, the optical gaps obtained in our work are 2.34 eV, 2.44 eV, and 2.47 eV using B3LYP+water, B3LYP+vacuum, and HSE06+crystal parameters, respectively, for the biggest size (2.76 nm) pristine quantum dot (6-Pris).

In brief, the triangular shaped $hg - C_3N_4$ QD structures are designed using a bottom-up approach. Starting from a single heptazine unit, we combined more such units at the edges (by replacing one of the edge hydrogen atoms) in a way to form larger triangular structures. Our calculations of the optical properties of the considered triangular shaped $hg - C_3N_4$ QDs suggest them to be size dependent. The UV-vis absorption spectra get red shifted with the increase in the size of the QDs due to the decrease in the optical gap. Chemical functionalization of the $hg - C_3N_4$ QDs resulted in the shifts of the most intense peaks in the absorption spectra compared to their pristine counterpart. Some of the functionalized

structures undergo a red shift, while some others experience a blue shift. In addition, the functionalization of all the considered hg - C_3N_4 QDs extended the absorption range covered by their corresponding pristine structures. Therefore, edge-functionalization is an effective approach to enhance the photophysical properties of hg - C_3N_4 QDs by tuning their absorption ranges to make them more suitable for utilization of the solar energy. The significant reduction in band gap with the increasing size and a better optical response also make them potential candidate for photocatalytic applications.

IV. CONCLUSION

To summarize, in this work we have presented an exhaustive first-principles DFT-based study of the electronic, vibrational, and optical properties of pristine and functionalized quantum dots of a novel 2D material g - C_3N_4 . Triangular structures of increasing sizes derived from heptazine were considered, and their geometries were optimized, followed by a check of their dynamic stability by performing a detailed vibrational frequency analysis. Additionally, the Raman spectrum of each considered structure was computed and analyzed. Electronic properties, such as the HOMO-LUMO energy gap, and the charge transfer were also studied, and it was observed that the edge-functionalization is an effective way of tuning the electronic properties of the hg - C_3N_4 QDs. Further, the influence of functionalization was also studied by comparing both the partial and total density of states of the functionalized and pristine structures.

Using the TD-DFT methodology, the UV-vis absorption spectra of all the structures were computed and analyzed in detail using two different hybrid functionals with different conditions. We found that most of the ultraviolet region gets covered in the pristine structures itself, which gets shifted to the visible region in the case of $6 - Pris$ QD due to the increase in size. Edge functionalization further extended the absorption range covered by the corresponding pristine structures suggesting that the edge-functionalized hg - C_3N_4 QDs will operate in a wide energy range and will be effective in enhancing the efficiency of solar cells. Moreover, their excellent optical properties make them a potential candidate for other optoelectronic devices such as light-emitting diodes operating both in the visible and ultraviolet range. Our results for the UV-vis spectra obtained in the case of carboxylic and hydroxyl groups are consistent with those obtained experimentally. Consequently, we hope

that this theoretical study of the absorption spectra of edge functionalized $hg - C_3N_4$ QDs using other functional groups will guide future experimental endeavors. Also our idea of using two different functionals and three different environmental parameters (vacuum, water, and crystalline environment) to explore their optical properties will be helpful for various experimental studies.

CONFLICTS OF INTEREST

There are no conflicts of interest to declare.

ACKNOWLEDGMENTS

One of the authors, K.D. acknowledges financial assistance from Prime Minister Research Fellowship (PMRF award ID-1302054). V.R. acknowledges the support through the Institute Post-Doctoral Fellowship (IPDF) of Indian Institute of Technology Bombay.

-
- [1] K. S. Novoselov, A. K. Geim, S. V. Morozov, D.-e. Jiang, Y. Zhang, S. V. Dubonos, I. V. Grigorieva, and A. A. Firsov, "Electric field effect in atomically thin carbon films," *Sci*, vol. 306, pp. 666–669, 2004.
 - [2] A. K. Geim and K. S. Novoselov, "The rise of graphene," *Nat. Mater*, vol. 6, pp. 183–191, 2007.
 - [3] P. Vogt, P. De Padova, C. Quaresima, J. Avila, E. Frantzeskakis, M. C. Asensio, A. Resta, B. Ealet, and G. Le Lay, "Silicene: compelling experimental evidence for graphenelike two-dimensional silicon," *Physical review letters*, vol. 108, no. 15, p. 155501, 2012.
 - [4] A. H. Woomer, T. W. Farnsworth, J. Hu, R. A. Wells, C. L. Donley, and S. C. Warren, "Phosphorene: synthesis, scale-up, and quantitative optical spectroscopy," *ACS nano*, vol. 9, no. 9, pp. 8869–8884, 2015.
 - [5] P. Singla, N. Goel, S. Singhal, *et al.*, "Boron nitride nanomaterials with different morphologies: synthesis, characterization and efficient application in dye adsorption," *Ceramics International*, vol. 41, no. 9, pp. 10565–10577, 2015.

- [6] Y. Yu, Q. Zhou, and J. Wang, "The ultra-rapid synthesis of 2d graphitic carbon nitride nanosheets via direct microwave heating for field emission," *Chemical Communications*, vol. 52, no. 16, pp. 3396–3399, 2016.
- [7] Z.-Y. Gao, W. Xu, Y. Gao, R. Guzman, H. Guo, X. Wang, Q. Zheng, Z. Zhu, Y.-Y. Zhang, X. Lin, *et al.*, "Experimental realization of atomic monolayer si9c15," *Advanced Materials*, vol. 34, no. 35, p. 2204779, 2022.
- [8] G. R. Bhimanapati, Z. Lin, V. Meunier, Y. Jung, J. Cha, S. Das, D. Xiao, Y. Son, M. S. Strano, V. R. Cooper, *et al.*, "Recent advances in two-dimensional materials beyond graphene," *ACS nano*, vol. 9, no. 12, pp. 11509–11539, 2015.
- [9] G. A. Naikoo, F. Arshad, M. Almas, I. U. Hassan, M. Z. Pedram, A. A. Aljabali, V. Mishra, Á. Serrano-Aroca, M. Birkett, N. B. Charbe, *et al.*, "2d materials, synthesis, characterization and toxicity: A critical review," *Chemico-Biological Interactions*, p. 110081, 2022.
- [10] H. L. Zhuang, A. K. Singh, and R. G. Hennig, "Computational discovery of single-layer III-V materials," *Phys. Rev. B*, vol. 87, p. 165415, 2013.
- [11] J. Li, J. Liu, C.-W. Wei, B. Liu, M. O'Donnell, and X. Gao, "Emerging applications of conjugated polymers in molecular imaging," *Phys. Chem. Chem. Phys.*, vol. 15, pp. 17006–17015, 2013.
- [12] Y.-J. Cheng, S.-H. Yang, and C.-S. Hsu, "Synthesis of conjugated polymers for organic solar cell applications," *Chem. Rev.*, vol. 109, pp. 5868–5923, 2009.
- [13] X. Qi, C. Tan, J. Wei, and H. Zhang, "Synthesis of graphene–conjugated polymer nanocomposites for electronic device applications," *Nanoscale*, vol. 5, pp. 1440–1451, 2013.
- [14] V. Kumar, K. Sharma, R. Sehgal, and S. Kalia, *Conjugated Polymers for Next-Generation Applications, Volume 2: Energy Storage Devices*. Woodhead Publishing, 2022.
- [15] J. F. Mike and J. L. Lutkenhaus, "Recent advances in conjugated polymer energy storage," *J. Polym. Sci. B: Polym. Phys.*, vol. 51, pp. 468–480, 2013.
- [16] Y. Zheng, Y. Jiao, Y. Zhu, L. H. Li, Y. Han, Y. Chen, A. Du, M. Jaroniec, and S. Z. Qiao, "Hydrogen evolution by a metal-free electrocatalyst," *Nature communications*, vol. 5, pp. 1–8, 2014.
- [17] G. Zhang, Z.-A. Lan, and X. Wang, "Conjugated polymers: catalysts for photocatalytic hydrogen evolution," *Angew. Chem. Int. Ed.*, vol. 55, pp. 15712–15727, 2016.

- [18] X. Wang, G. Sun, N. Li, and P. Chen, "Quantum dots derived from two-dimensional materials and their applications for catalysis and energy," *Chem. Soc. Rev.*, vol. 45, pp. 2239–2262, 2016.
- [19] Z. Zhang, K. Leinenweber, M. Bauer, L. A. J. Garvie, P. F. McMillan, and G. H. Wolf, "High-pressure bulk synthesis of crystalline C_3N_4 : A novel C_3N_4 graphitic derivative," *Journal of the American Chemical Society*, vol. 123, no. 32, pp. 7788–7796, 2001. PMID: 11493052.
- [20] A. Wang, C. Wang, L. Fu, W. Wong-Ng, and Y. Lan, "Recent advances of graphitic carbon nitride-based structures and applications in catalyst, sensing, imaging, and leds," *Nano-micro letters*, vol. 9, pp. 1–21, 2017.
- [21] M. Ismael and Y. Wu, "A mini-review on the synthesis and structural modification of g- C_3N_4 -based materials, and their applications in solar energy conversion and environmental remediation," *Sustain. Energy Fuels*, vol. 3, pp. 2907–2925, 2019.
- [22] Y. Xu and S.-P. Gao, "Band gap of C_3N_4 in the gw approximation," *International Journal of Hydrogen Energy*, vol. 37, no. 15, pp. 11072–11080, 2012. Hydrogen Enriched Methane.
- [23] X. Wang, K. Maeda, A. Thomas, K. Takanabe, G. Xin, J. M. Carlsson, K. Domen, and M. Antonietti, "A metal-free polymeric photocatalyst for hydrogen production from water under visible light," *Nature Materials*, vol. 8, pp. 76–80, Jan 2009.
- [24] W. K. Darkwah and Y. Ao, "Mini review on the structure and properties (photocatalysis), and preparation techniques of graphitic carbon nitride nano-based particle, and its applications," *Nanoscale Res. Lett.*, vol. 13, pp. 1–15, 2018.
- [25] S. Huang, J. Lang, C. Du, F. Bian, Y. Su, and X. Wang, "Enhanced driving force and charge separation efficiency in disordered C_3N_4 : boosting photocatalytic activity toward water reduction," *Chem. Eng. J.*, vol. 309, pp. 313–320, 2017.
- [26] X. Zhang, X. Xie, H. Wang, J. Zhang, B. Pan, and Y. Xie, "Enhanced photoresponsive ultrathin graphitic-phase C_3N_4 nanosheets for bioimaging," *J. Am. Chem. Soc.*, vol. 135, pp. 18–21, 2013.
- [27] G. Dong, Y. Zhang, Q. Pan, and J. Qiu, "A fantastic graphitic carbon nitride (g- C_3N_4) material: electronic structure, photocatalytic and photoelectronic properties," *J. Photochem. Photobiol. C: Photochem. Rev.*, vol. 20, pp. 33–50, 2014.
- [28] S. Patnaik, D. P. Sahoo, and K. Parida, "An overview on Ag modified g- C_3N_4 based nanostructured materials for energy and environmental applications," *Renew. Sustain. Energy Rev.*, vol. 82, pp. 1297–1312, 2018.

- [29] Y. Tian, B. Chang, Z. Yang, B. Zhou, F. Xi, and X. Dong, "Graphitic carbon nitride–BiVO₄ heterojunctions: simple hydrothermal synthesis and high photocatalytic performances," *RSC Adv.*, vol. 4, pp. 4187–4193, 2014.
- [30] M. Majdoub, Z. Anfar, and A. Amedlous, "Emerging chemical functionalization of g-C₃N₄: covalent/noncovalent modifications and applications," *ACS Nano*, vol. 14, pp. 12390–12469, 2020.
- [31] S. Ullah, P. A. Denis, M. G. Menezes, F. Sato, and R. B. Capaz, "Electronic properties of substitutional impurities in graphene like C₂N, tg-C₃N₄, and hg-C₃N₄," *Phys. Rev. B*, vol. 102, p. 134112, 2020.
- [32] X. Chen, W. Xu, J. Jin, P. Wang, B. Song, and P. He, "Effect of B and O doping on the electronic structure and quantum capacitance of carbon nitride monolayers using first-principles calculations," *J. Appl. Phys.*, vol. 129, p. 174301, 2021.
- [33] X. Yang, L. Zhao, S. Wang, J. Li, and B. Chi, "Recent progress of g-c3n4 applied in solar cells," *Journal of Materiomics*, vol. 7, no. 4, pp. 728–741, 2021.
- [34] S.-Y. Li and L. He, "Recent progresses of quantum confinement in graphene quantum dots," *Frontiers of Physics*, vol. 17, p. 33201, Nov 2021.
- [35] Q. Xu, Y. Niu, J. Li, Z. Yang, J. Gao, L. Ding, H. Ni, P. Zhu, Y. Liu, Y. Tang, Z.-P. Lv, B. Peng, T. S. Hu, H. Zhou, and C. Xu, "Recent progress of quantum dots for energy storage applications," *Carbon Neutrality*, vol. 1, p. 13, Apr 2022.
- [36] M. Ghashghaee, Z. Azizi, and M. Ghambarian, "Conductivity tuning of charged triazine and heptazine graphitic carbon nitride (g-C₃N₄) quantum dots via nonmetal (B, O, S, P) doping: DFT calculations," *J. Phys. Chem. Solids*, vol. 141, p. 109422, 2020.
- [37] Y. Wang, X. Wang, and M. Antonietti, "Polymeric graphitic carbon nitride as a heterogeneous organocatalyst: from photochemistry to multipurpose catalysis to sustainable chemistry," *Angew. Chem. Int. Ed.*, vol. 51, pp. 68–89, 2012.
- [38] M. Ghashghaee, Z. Azizi, and M. Ghambarian, "Adsorption of iron (II, III) cations on pristine heptazine and triazine polymeric carbon nitride quantum dots of buckled and planar structures: theoretical insights," *Adsorption*, vol. 26, pp. 429–442, 2020.
- [39] M. Ghashghaee, Z. Azizi, and M. Ghambarian, "Quantum-chemical calculations on graphitic carbon nitride (g-C₃N₄) single-layer nanostructures: polymeric slab vs. quantum dot," *J. Struct. Chem.*, vol. 31, pp. 1137–1148, 2020.

- [40] O. P. Olademehin, T. L. Ellington, and K. L. Shuford, "Toward quantum confinement in graphitic carbon nitride-based polymeric monolayers," *The Journal of Physical Chemistry A*, vol. 125, pp. 7597–7606, Sep 2021.
- [41] N. Ullah, S. Chen, and R. Zhang, "Mechanism of charge separation and frontier orbital structure in graphitic carbon nitride and graphene quantum dots," *ChemPhysChem*, vol. 19, no. 19, pp. 2534–2539, 2018.
- [42] J. Wu, S. Yang, J. Li, Y. Yang, G. Wang, X. Bu, P. He, J. Sun, J. Yang, Y. Deng, *et al.*, "Electron injection of phosphorus doped g-C₃N₄ quantum dots: Controllable photoluminescence emission wavelength in the whole visible light range with high quantum yield," *Adv. Opt. Mater.*, vol. 4, pp. 2095–2101, 2016.
- [43] A. Bandyopadhyay, D. Ghosh, N. M. Kaley, and S. K. Pati, "Photocatalytic activity of g-C₃N₄ quantum dots in visible light: effect of physicochemical modifications," *J. Phys. Chem. C*, vol. 121, pp. 1982–1989, 2017.
- [44] S. Zhai, P. Guo, J. Zheng, P. Zhao, B. Suo, and Y. Wan, "Density functional theory study on the stability, electronic structure and absorption spectrum of small size g-C₃N₄ quantum dots," *Comput. Mater. Sci.*, vol. 148, pp. 149–156, 2018.
- [45] J. Zhou, Y. Yang, and C.-y. Zhang, "A low-temperature solid-phase method to synthesize highly fluorescent carbon nitride dots with tunable emission," *Chem. Commun.*, vol. 49, pp. 8605–8607, 2013.
- [46] Z. Zhou, Y. Shen, Y. Li, A. Liu, S. Liu, and Y. Zhang, "Chemical cleavage of layered carbon nitride with enhanced photoluminescent performances and photoconduction," *ACS Nano*, vol. 9, pp. 12480–12487, 2015.
- [47] Y. Li, H. Shu, X. Niu, and J. Wang, "Electronic and optical properties of edge-functionalized graphene quantum dots and the underlying mechanism," *J. Phys. Chem. C*, vol. 119, pp. 24950–24957, 2015.
- [48] P. Hohenberg and W. Kohn, "Inhomogeneous electron gas," *Phys. Rev.*, vol. 136, p. B864, 1964.
- [49] W. Kohn and L. J. Sham, "Self-consistent equations including exchange and correlation effects," *Phys. Rev.*, vol. 140, p. A1133, 1965.
- [50] M. e. Frisch, G. Trucks, H. Schlegel, G. Scuseria, M. Robb, J. Cheeseman, G. Scalmani, V. Barone, G. Petersson, H. Nakatsuji, *et al.*, "Gaussian 16," 2016.

- [51] A. D. Becke, "Density-functional thermochemistry. i. the effect of the exchange-only gradient correction," *J. Chem. Phys.*, vol. 96, pp. 2155–2160, 1992.
- [52] R. Krishnan, J. S. Binkley, R. Seeger, and J. A. Pople, "Self-consistent molecular orbital methods. xx. a basis set for correlated wave functions," *J. Chem. Phys.*, vol. 72, pp. 650–654, 1980.
- [53] R. Dennington, T. Keith, J. Millam, *et al.*, "Gaussview, version 6," 2009.
- [54] T. Lu and F. Chen, "Multiwfn: a multifunctional wavefunction analyzer," *J. Comput. Chem.*, vol. 33, pp. 580–592, 2012.
- [55] E. Runge and E. K. Gross, "Density-functional theory for time-dependent systems," *Phys. Rev. Lett.*, vol. 52, p. 997, 1984.
- [56] M. E. Casida, "Time-dependent density-functional theory for molecules and molecular solids," *J MOL STRUC-THEOCHEM*, vol. 914, pp. 3–18, 2009.
- [57] S. MiertuÅ, E. Scrocco, and J. Tomasi, "Electrostatic interaction of a solute with a continuum. a direct utilizaion of ab initio molecular potentials for the prevision of solvent effects," *Chemical Physics*, vol. 55, no. 1, pp. 117–129, 1981.
- [58] D. M. Chipman, "Comparison of solvent reaction field representations," *Theor. Chem. Acc.*, vol. 107, pp. 80–89, 2002.
- [59] I. Fleming, "Frontier orbitals and organic chemical reactions 1976," *Willey and Sons, London*, 1982.
- [60] K. Houk, "Applications of frontier molecular orbital theory to pericyclic reactions," in *Organic Chemistry: A Series of Monographs*, vol. 35, pp. 181–271, Elsevier, 1977.
- [61] H. Tetsuka, "Nitrogen-functionalized graphene quantum dots: A versatile platform for integrated optoelectronic devices," *Chem. Rec.*, vol. 20, pp. 429–439, 2020.
- [62] K. F. Mak, H. Felipe, K. He, J. Deslippe, N. Petrone, J. Hone, J. Shan, S. G. Louie, and T. F. Heinz, "Tuning many-body interactions in graphene: The effects of doping on excitons and carrier lifetimes," *Phys. Rev. Lett.*, vol. 112, p. 207401, 2014.
- [63] W. Wang, C. Y. Jimmy, Z. Shen, D. K. Chan, and T. Gu, "g-C₃N₄ quantum dots: direct synthesis, upconversion properties and photocatalytic application," *Chem. Commun.*, vol. 50, pp. 10148–10150, 2014.
- [64] Z. Liu, T. Lu, and Q. Chen, "An sp-hybridized all-carboatomic ring, cyclo[18]carbon: Electronic structure, electronic spectrum, and optical nonlinearity," *Carbon*, vol. 165, pp. 461–467, 2020.

- [65] Y. Li, J. Cai, F. Liu, H. Yu, F. Lin, H. Yang, Y. Lin, and S. Li, "Highly crystalline graphitic carbon nitride quantum dots as a fluorescent probe for detection of fe(iii) via an inner filter effect," *Microchimica Acta*, vol. 185, p. 134, Jan 2018.
- [66] Z. Zheng, D. A. Egger, J.-L. Brédas, L. Kronik, and V. Coropceanu, "Effect of solid-state polarization on charge-transfer excitations and transport levels at organic interfaces from a screened range-separated hybrid functional," *The Journal of Physical Chemistry Letters*, vol. 8, pp. 3277–3283, Jul 2017.
- [67] H. Sun, S. Ryno, C. Zhong, M. K. Ravva, Z. Sun, T. Körzdörfer, and J.-L. Brédas, "Ionization energies, electron affinities, and polarization energies of organic molecular crystals: Quantitative estimations from a polarizable continuum model (pcm)-tuned range-separated density functional approach," *Journal of Chemical Theory and Computation*, vol. 12, pp. 2906–2916, Jun 2016.
- [68] P. C. Patra and Y. N. Mohapatra, "Dielectric constant of thin film graphitic carbon nitride (g-C₃N₄) and double dielectric Al₂O₃/g-C₃N₄," *Applied Physics Letters*, vol. 118, p. 103501, 03 2021.

Supporting Information for
Tuning the electronic and optical properties of hg-C₃N₄ quantum dots with edge-functionalization: A computational perspective

Khushboo Dange, Vaishali Roonthe, and Alok Shukla*

*Department of Physics, Indian Institute of Technology Bombay, Powai, Mumbai
400076, India*

This supporting information is divided into four sections. The first section contains the calculated bond lengths and bond angles for the considered structures. The second section contains the discussion on their Raman spectra and some unique vibrational modes. The third section contains the plots of total density of states (TDOS) and partial density of states (PDOS) for the pristine and edge-functionalized hg-C₃N₄ QDs. The last section contains the UV-vis absorption spectra for all the pristine structures and the information related to the excited states contributing to the most intense peaks in the absorption spectra as well as the first excited state of all the structures considered in this work.

A. Bond lengths and bond angles

Table S1: Calculated bond lengths and bond angles for the atoms that are nearby the attached functional groups for all the considered structures.

Structure	Bond Lengths	Cal. (Å)	Bond Angles	Cal. (°)	Structure	Bond Lengths	Cal. (Å)	Bond Angles	Cal. (°)
1-Pris	C4-N16	1.35	N16-C4-N8	116.0	4-COOH	C33-N43	1.38	N43-C33-N36	119.3
	C4-N8	1.34	N16-C4-N7	116.0		C33-N37	1.34	N43-C33-N37	112.1
	C4-N7	1.34	N7-C4-N8	127.9		C33-N36	1.33	N37-C33-N36	128.6
1-CH ₃	C4-N16	1.35	N16-C4-N8	114.8	4-OH	C33-N43	1.34	N43-C33-N36	114.6
	C4-N8	1.34	N16-C4-N7	117.8		C33-N37	1.35	N43-C33-N37	116.5
	C4-N7	1.35	N7-C4-N8	127.4		C33-N36	1.39	N37-C33-N36	128.8
1-CHO	C4-N16	1.38	N16-C4-N8	112.2	4-F	C33-N43	1.38	N43-C33-N36	118.3
	C4-N8	1.34	N16-C4-N7	119.1		C33-N37	1.33	N43-C33-N37	111.8
	C4-N7	1.32	N7-C4-N8	128.7		C33-N36	1.34	N37-C33-N36	129.7
1-COCH ₃	C4-N16	1.38	N16-C4-N8	112.0	5-Pris	C50-N62	1.34	N62-C50-N59	115.9
	C4-N8	1.34	N16-C4-N7	119.6		C50-N61	1.35	N62-C50-N61	115.9
	C4-N7	1.33	N7-C4-N8	128.4		C50-N59	1.35	N61-C50-N59	128.1
1-COOH	C4-N16	1.38	N16-C4-N8	112.0	5-CH ₃	C50-N62	1.34	N62-C50-N59	117.7
	C4-N8	1.34	N16-C4-N7	119.3		C50-N61	1.35	N62-C50-N61	117.7
	C4-N7	1.33	N7-C4-N8	128.7		C50-N59	1.35	N61-C50-N59	127.5

1-OH	C4-N16	1.35	N16-C4-N8	116.5	5-CHO	C50-N62	1.38	N62-C50-N59	118.9
	C4-N8	1.34	N16-C4-N7	114.7		C50-N61	1.34	N62-C50-N61	112.2
	C4-N7	1.34	N7-C4-N8	128.8		C50-N59	1.33	N61-C50-N59	128.8
1-F	C4-N16	1.39	N16-C4-N8	111.7	5-COCH ₃	C50-N62	1.38	N62-C50-N59	119.5
	C4-N8	1.34	N16-C4-N7	118.3		C50-N61	1.35	N62-C50-N61	112.0
	C4-N7	1.32	N7-C4-N8	129.8		C50-N59	1.33	N61-C50-N59	128.5
3-Pris	C18-N30	1.34	N30-C18-N27	115.9	5-COOH	C50-N62	1.38	N62-C50-N59	119.1
	C18-N27	1.35	N30-C18-N29	116.0		C50-N61	1.34	N62-C50-N61	112.1
	C18-N29	1.35	N27-C18-N29	128.0		C50-N59	1.33	N61-C50-N59	128.8
3-CH ₃	C18-N30	1.34	N30-C18-N27	114.7	5-OH	C50-N62	1.34	N62-C50-N59	114.6
	C18-N27	1.35	N30-C18-N29	117.8		C50-N61	1.34	N62-C50-N61	116.4
	C18-N29	1.35	N27-C18-N29	127.4		C50-N59	1.35	N61-C50-N59	129.0
3-CHO	C18-N30	1.38	N30-C18-N27	112.2	5-F	C50-N62	1.38	N62-C50-N59	118.2
	C18-N27	1.35	N30-C18-N29	119.0		C50-N61	1.34	N62-C50-N61	111.7
	C18-N29	1.33	N27-C18-N29	128.7		C50-N59	1.33	N61-C50-N59	129.9
3-COCH ₃	C18-N30	1.38	N30-C18-N27	112.0	6-Pris	C85-N97	1.34	N97-C85-N89	116.1
	C18-N27	1.35	N30-C18-N29	119.5		C85-N88	1.35	N97-C85-N88	115.9
	C18-N29	1.33	N27-C18-N29	128.4		C85-N89	1.35	N89-C85-N88	128.0
3-COOH	C18-N30	1.38	N30-C18-N27	112.0	6-CH ₃	C85-N97	1.34	N97-C85-N89	117.9
	C18-N27	1.35	N30-C18-N29	119.3		C85-N88	1.35	N97-C85-N88	114.7
	C18-N29	1.33	N27-C18-N29	128.7		C85-N89	1.35	N89-C85-N88	127.4
3-OH	C18-N30	1.34	N30-C18-N27	116.4	6-CHO	C85-N97	1.38	N97-C85-N89	119.0
	C18-N27	1.35	N30-C18-N29	114.6		C85-N88	1.35	N97-C85-N88	112.3
	C18-N29	1.35	N27-C18-N29	128.9		C85-N89	1.33	N89-C85-N88	128.7
3-F	C18-N30	1.38	N30-C18-N27	111.7	6-COCH ₃	C85-N97	1.38	N97-C85-N89	119.6
	C18-N27	1.34	N30-C18-N29	118.4		C85-N88	1.35	N97-C85-N88	112.6
	C18-N29	1.33	N27-C18-N29	129.8		C85-N89	1.33	N89-C85-N88	128.4
4-Pris	C33-N43	1.34	N43-C33-N36	116.0	6-COOH	C85-N97	1.38	N97-C85-N89	119.3
	C33-N37	1.35	N43-C33-N37	116.0		C85-N88	1.35	N97-C85-N88	112.6
	C33-N36	1.35	N37-C33-N36	128.0		C85-N89	1.33	N89-C85-N88	128.6
4-CH ₃	C33-N43	1.35	N43-C33-N36	117.8	6-OH	C85-N97	1.34	N97-C85-N89	114.6
	C33-N37	1.35	N43-C33-N37	114.8		C85-N88	1.35	N97-C85-N88	116.4
	C33-N36	1.34	N37-C33-N36	127.4		C85-N89	1.35	N89-C85-N88	128.9
4-CHO	C33-N43	1.38	N43-C33-N36	119.0	6-F	C85-N97	1.38	N97-C85-N89	118.4
	C33-N37	1.34	N43-C33-N37	112.3		C85-N88	1.34	N97-C85-N88	111.7
	C33-N36	1.33	N37-C33-N36	128.6		C85-N89	1.33	N89-C85-N88	129.8
4-COCH ₃	C33-N43	1.38	N43-C33-N36	119.6					
	C33-N37	1.35	N43-C33-N37	112.1					
	C33-N36	1.33	N37-C33-N36	128.3					

B. Vibrational Properties: Raman Spectra

The computed Raman spectra corresponding to each of the considered structures is depicted in Fig. S1. The peaks in each of the plots can be classified into two regions: (i) the low-intensity region and (ii) the high-intensity region. As shown in Fig. S1(b), the low intensity peaks for all the considered 3-X structures fall in the frequency range 700–1700 cm⁻¹, which arise mostly due to the deformation of C–N bonds because of their stretching and scissoring modes. In the frequency range 3000–4000 cm⁻¹, peaks arise due to stretching vibrations of the N–H bonds, with the highest intensity near 3600 cm⁻¹. In addition to these, peaks corresponding to unique vibrational modes of the bonds

of the attached functional groups are also present in the spectra of functionalized hg-C₃N₄ QDs. In the Raman spectra of 3-CH₃ QD, stretching of the C-H bonds (of -CH₃) gives rise to a peak at 3000 cm⁻¹. For 3-CHO QD, vibrations due to stretching of C=O and C-H bonds are also present at the frequencies 1840 cm⁻¹ and 2920 cm⁻¹, respectively. Similarly, in the case of 3-COCH₃ structure, stretching of the C=O bond occurs at 1837 cm⁻¹ whereas stretching of the C-H bonds occur in the frequency range 3000–3100 cm⁻¹. In the case of 3-COOH structure, vibrations due to the attached functional group are present around 1870 cm⁻¹ which include stretching of the C=O and O-H bonds as well as scissoring of the O-C=O bond. In the Raman spectra of 3-OH and 3-F QDs, peaks around 3500 cm⁻¹ correspond to stretching of the O-H and O-F bonds, respectively. The Raman spectra of other pristine hg-C₃N₄ QDs and their associated functionalized structures exhibit similar type of qualitative behavior, as illustrated in Figs. S1(a), (c), (d), and (e).

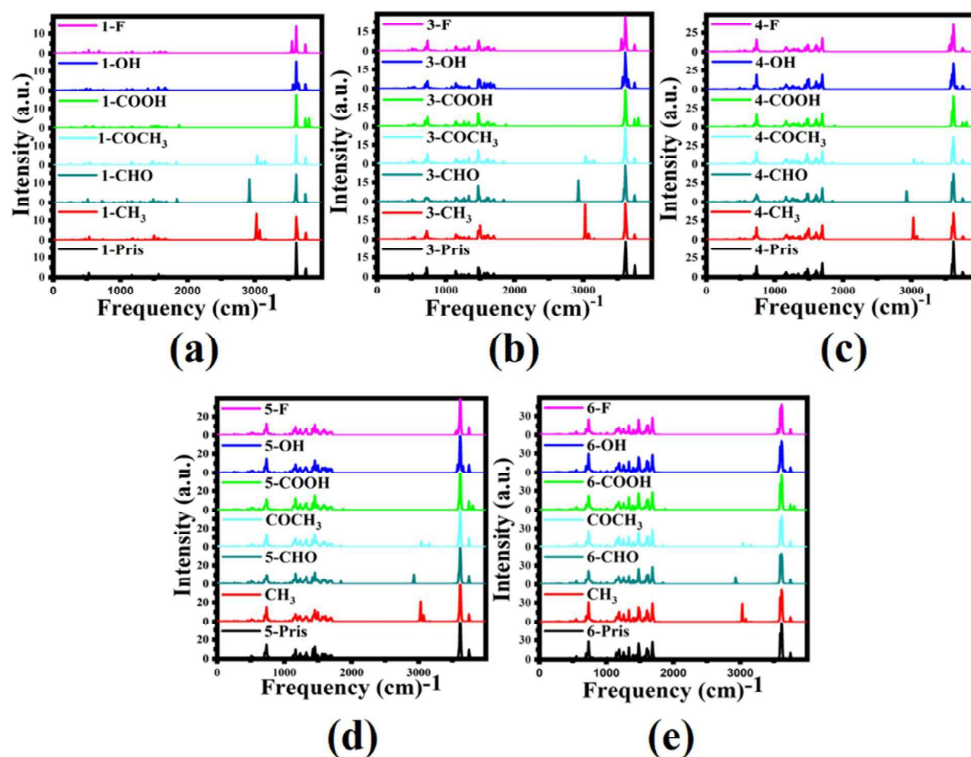


Figure S1: Raman spectra plots of (a) 1-X, (b) 3-X, (c) 4-X, (d) 5-X, and (e) 6-X structures. X represents the attached functional groups (-Pris, -CH₃, -CHO, -COCH₃, -COOH, -OH, and -F).

C. Total and partial density of states plots for the considered hg-C₃N₄ quantum dots

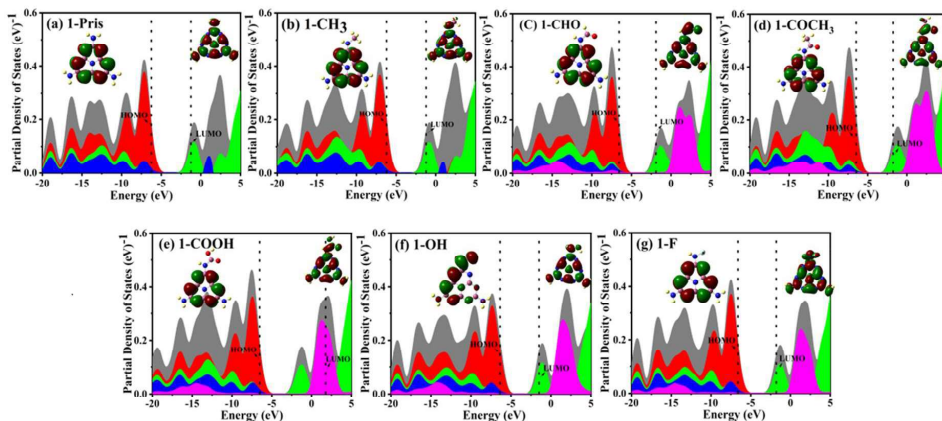


Figure S2: TDOS and PDOS plots of (a) 1-Pris, (b) 1-CH₃, (c) 1-CHO, (d) 1-COCH₃, (e) 1-COOH, (f) 1-OH, and (g) 1-F structures. Grey represents the TDOS. Red, green, blue, and magenta colors represent the contributions of H, N, C, and O or F atoms, respectively. Corresponding HOMO and LUMO are shown in the inset of each plot.

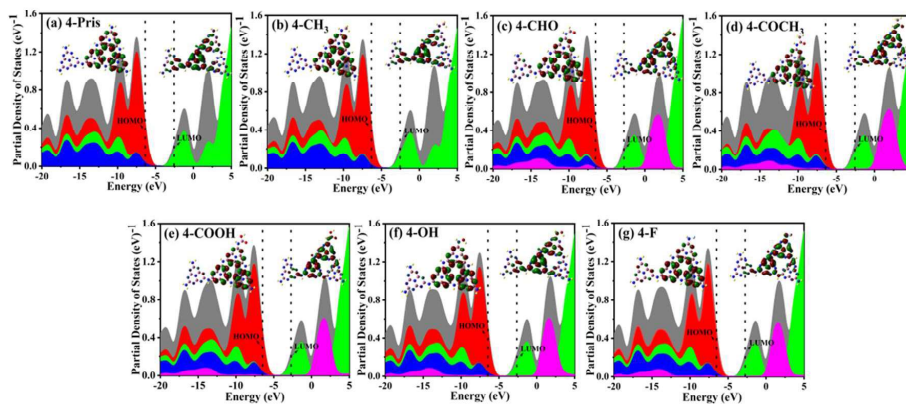


Figure S3: TDOS and PDOS plots of (a) 4-Pris, (b) 4-CH₃, (c) 4-CHO, (d) 4-COCH₃, (e) 4-COOH, (f) 4-OH, and (g) 4-F structures. Grey represents the TDOS. Red, green, blue, and magenta colors represent the contributions of H, N, C, and O or F atoms, respectively. Corresponding HOMO and LUMO are shown in the inset of each plot.

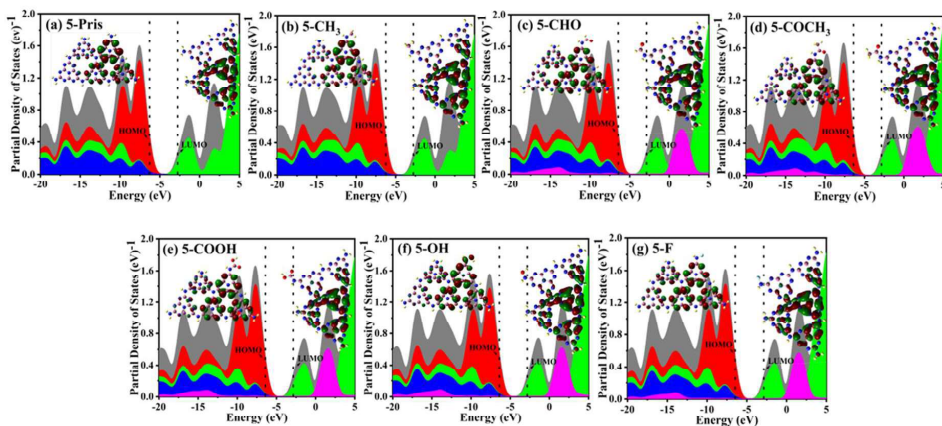


Figure S4: TDOS and PDOS plots of (a) 5-Pris, (b) 5-CH₃, (c) 5-CHO, (d) 5-COCH₃, (e) 5-COOH, (f) 5-OH, and (g) 5-F structures. Grey represents the TDOS. Red, green, blue, and magenta colors represent the contributions of H, N, C, and O or F atoms, respectively. Corresponding HOMO and LUMO are shown in the inset of each plot.

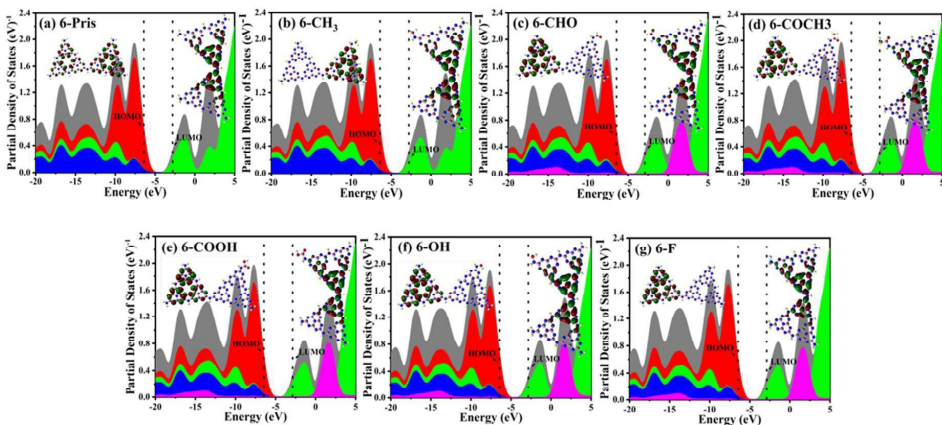


Figure S5: TDOS and PDOS plots of (a) 6-Pris, (b) 6-CH₃, (c) 6-CHO, (d) 6-COCH₃, (e) 6-COOH, (f) 6-OH, and (g) 6-F structures. Grey represents the TDOS. Red, green, blue, and magenta colors represent the contributions of H, N, C, and O or F atoms, respectively. Corresponding HOMO and LUMO are shown in the inset of each plot.

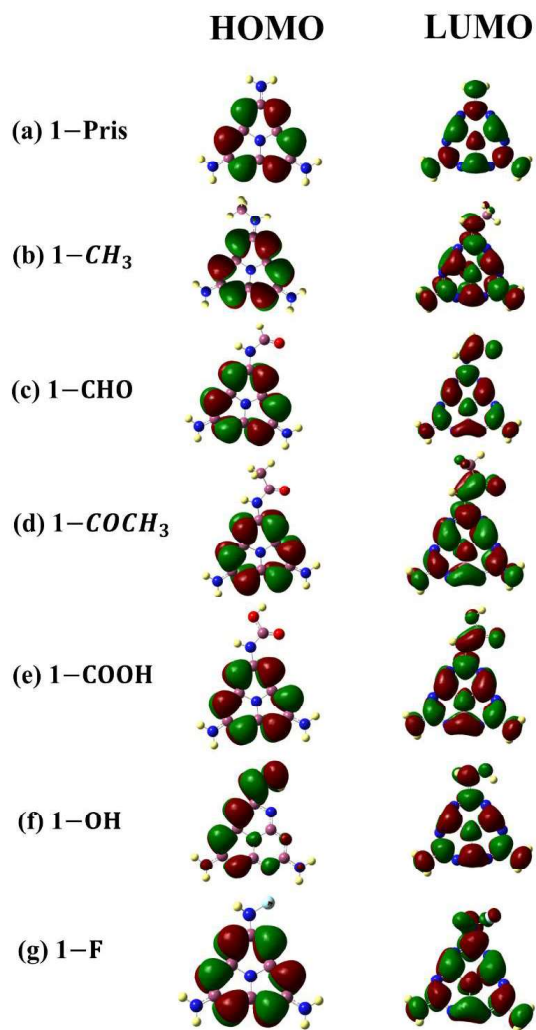


Figure S6: HOMO and LUMO plots for the 1-X structures obtained using HSE06 functional.

D. UV-vis absorption spectra, TD-DFT wave functions, and spatial distribution of photo-induced electrons and holes

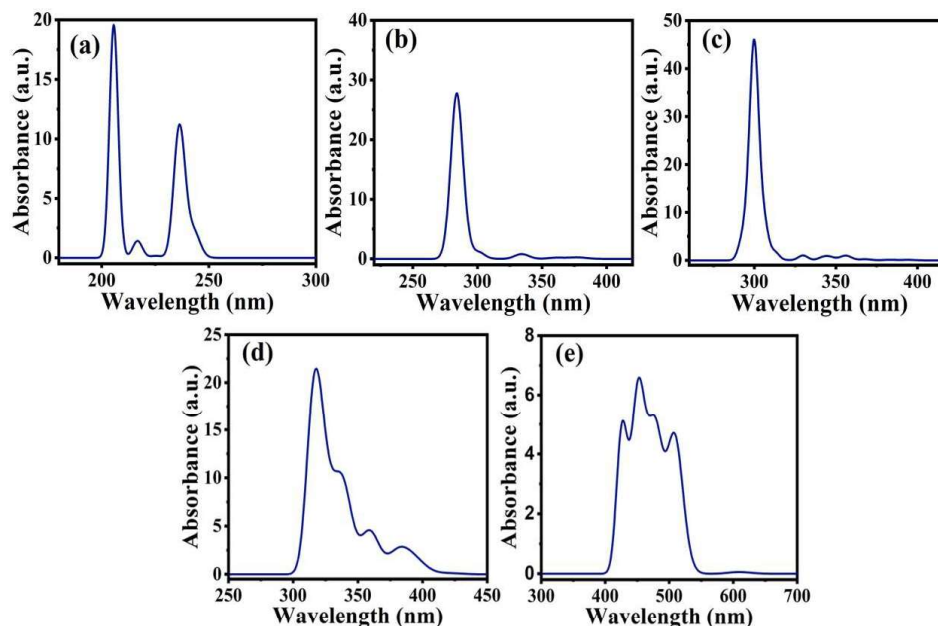


Figure S7: UV-vis absorption spectra of (a) 1-Pris, (b) 3-Pris, (c) 4-Pris, (d) 5-Pris, and (e) 6-Pris structures.

Table S2: TD-DFT wave functions, excitation energies (E_x) and oscillator strengths (f) corresponding to the most intense peaks in the absorption spectra of “1-X” hg- C_3N_4 Qds. Below a configuration $H-m \rightarrow L+n$ implies a single excitation from the HOMO - m orbital to the LUMO + n orbital.

Structure	State	Configuration	Coefficient	E_x (eV)	f
1-Pris	20^1A	$ H-4 \rightarrow L+1\rangle$	0.5092	6.03 (205 nm)	1.02
		$ H-2 \rightarrow L+1\rangle$	-0.2173		
		$ H-1 \rightarrow L+1\rangle$	0.2170		
1-CH ₃	12^1A	$ H-1 \rightarrow L+1\rangle$	0.3398	5.95 (208 nm)	0.35
		$ H-1 \rightarrow L+2\rangle$	0.4118		
		$ H-4 \rightarrow L\rangle$	0.3195		
1-CHO	20^1A	$ H-3 \rightarrow L+2\rangle$	0.5623	5.93 (209 nm)	0.80
		$ H-1 \rightarrow L+1\rangle$	-0.3170		
		$ H \rightarrow L+1\rangle$	0.1383		
1-COCH ₃	13^1A	$ H-6 \rightarrow L\rangle$	0.6549	5.41 (229 nm)	0.56
		$ H-3 \rightarrow L+1\rangle$	0.1732		
		$ H-1 \rightarrow L+1\rangle$	0.1095		

1-COOH	14 ¹ A	$ H - 6 \rightarrow L\rangle$	0.6276	5.56 (223 nm)	0.57
		$ H - 2 \rightarrow L + 1\rangle$	0.2950		
1-OH	10 ¹ A	$ H - 1 \rightarrow L + 1\rangle$	0.3678	5.20 (238 nm)	0.37
		$ H - 1 \rightarrow L + 2\rangle$	-0.3248		
		$ H - 2 \rightarrow L\rangle$	-0.2989		
1-F	20 ¹ A	$ H - 2 \rightarrow L + 2\rangle$	0.3665	5.96 (208 nm)	1.00
		$ H - 4 \rightarrow L + 2\rangle$	0.3243		
		$ H - 5 \rightarrow L + 2\rangle$	0.3056		

Table S3: The same information as in Table S2 but for the “3-X” hg-C₃N₄ QDs.

Structure	State	Configuration	Coefficient	E _x (eV)	<i>f</i>
3-Pris	14 ¹ A	$ H - 6 \rightarrow L\rangle$	0.4449	4.36 (284 nm)	0.97
		$ H - 5 \rightarrow L + 1\rangle$	-0.3542		
		$ H - 4 \rightarrow L\rangle$	0.2579		
3-CH ₃	16 ¹ A	$ H - 6 \rightarrow L\rangle$	0.3937	4.38 (283 nm)	0.50
		$ H - 5 \rightarrow L\rangle$	0.2959		
		$ H - 6 \rightarrow L + 1\rangle$	-0.2192		
3-CHO	16 ¹ A	$ H - 3 \rightarrow L + 1\rangle$	0.3043	4.31 (287.7 nm)	0.85
		$ H - 5 \rightarrow L\rangle$	0.2917		
		$ H - 6 \rightarrow L + 1\rangle$	0.2527		
3-COCH ₃	16 ¹ A	$ H - 6 \rightarrow L + 1\rangle$	0.3656	4.32 (287 nm)	0.90
		$ H - 3 \rightarrow L + 1\rangle$	-0.3040		
		$ H - 7 \rightarrow L\rangle$	-0.2778		
3-COOH	15 ¹ A	$ H \rightarrow L + 3\rangle$	0.3280	4.31 (288 nm)	0.40
		$ H - 6 \rightarrow L\rangle$	0.3004		
		$ H - 3 \rightarrow L + 1\rangle$	-0.2949		
3-OH	17 ¹ A	$ H - 5 \rightarrow L\rangle$	0.3578	4.36 (284 nm)	0.80
		$ H - 6 \rightarrow L\rangle$	-0.2961		
		$ H - 6 \rightarrow L + 1\rangle$	-0.2479		
3-F	14 ¹ A	$ H \rightarrow L + 3\rangle$	0.3101	4.31 (287 nm)	0.50
		$ H - 5 \rightarrow L + 1\rangle$	-0.2843		
		$ H - 4 \rightarrow L\rangle$	-0.2595		

Table S4: The same information as in Table S2 but for the “4-X” hg-C₃N₄ QDs.

Structure	State	Configuration	Coefficient	E _x (eV)	<i>f</i>
4-Pris	16 ¹ A	$ H - 6 \rightarrow L + 1\rangle$	0.2821	4.14 (299 nm)	0.70
		$ H - 6 \rightarrow L\rangle$	0.2185		
		$ H - 7 \rightarrow L\rangle$	-0.1951		
4-CH ₃	18 ¹ A	$ H - 7 \rightarrow L\rangle$	0.4045	4.16 (298 nm)	1.3
		$ H - 8 \rightarrow L\rangle$	0.3146		
		$ H - 5 \rightarrow L\rangle$	-0.2475		
4-CHO	17 ¹ A	$ H - 4 \rightarrow L\rangle$	0.3253	4.12 (301 nm)	0.80
		$ H - 6 \rightarrow L + 1\rangle$	0.2513		
		$ H \rightarrow L + 3\rangle$	0.2075		
4-COCH ₃	17 ¹ A	$ H - 4 \rightarrow L\rangle$	0.2551	4.12 (301 nm)	1.00
		$ H - 7 \rightarrow L + 1\rangle$	0.2178		
		$ H - 6 \rightarrow L + 1\rangle$	-0.2066		

4-COOH	16 ¹ A	$ H - 6 \rightarrow L + 1\rangle$	0.3328	4.11 (301 nm)	1.30
		$ H - 6 \rightarrow L\rangle$	0.2526		
		$ H - 4 \rightarrow L\rangle$	-0.2338		
4-OH	18 ¹ A	$ H - 7 \rightarrow L\rangle$	0.3569	4.15 (298 nm)	1.26
		$ H - 6 \rightarrow L\rangle$	-0.2712		
		$ H - 9 \rightarrow L\rangle$	0.2109		
4-F	16 ¹ A	$ H - 6 \rightarrow L + 1\rangle$	0.3139	4.11 (301 nm)	1.20
		$ H - 4 \rightarrow L\rangle$	-0.2616		
		$ H - 6 \rightarrow L\rangle$	0.2527		

Table S5: The same information as in Table S2 but for the “5-X” hg-C₃N₄ QDs.

Structure	State	Configuration	Coefficient	E _x (eV)	<i>f</i>
5-Pris	15 ¹ A	$ H - 5 \rightarrow L + 1\rangle$	0.3091	3.90 (318 nm)	0.02
		$ H - 6 \rightarrow L + 1\rangle$	-0.2092		
		$ H - 5 \rightarrow L\rangle$	-0.1928		
5-CH ₃	14 ¹ A	$ H - 6 \rightarrow L\rangle$	0.3071	3.90 (318 nm)	0.03
		$ H - 6 \rightarrow L + 1\rangle$	-0.2400		
		$ H - 5 \rightarrow L + 1\rangle$	-0.1996		
5-CHO	17 ¹ A	$ H - 1 \rightarrow L + 3\rangle$	0.3216	3.92 (316 nm)	0.02
		$ H \rightarrow L + 3\rangle$	0.2912		
		$ H - 5 \rightarrow L\rangle$	0.2832		
5-COCH ₃	16 ¹ A	$ H - 10 \rightarrow L\rangle$	-0.2801	3.92 (316 nm)	0.03
		$ H - 3 \rightarrow L + 2\rangle$	-0.2305		
		$ H - 5 \rightarrow L + 1\rangle$	-0.2196		
5-COOH	18 ¹ A	$ H - 10 \rightarrow L\rangle \rightarrow$	0.3228	3.93 (315 nm)	0.04
		$ H \rightarrow L + 3\rangle$	0.2362		
		$ H - 6 \rightarrow L\rangle$	0.2345		
5-OH	13 ¹ A	$ H \rightarrow L + 2\rangle$	0.4466	3.88 (319 nm)	0.04
		$ H - 2 \rightarrow L + 1\rangle$	-0.2895		
		$ H - 3 \rightarrow L + 1\rangle$	-0.2504		
5-F	18 ¹ A	$ H - 10 \rightarrow L\rangle$	0.3333	3.93 (315 nm)	0.05
		$ H - 6 \rightarrow L\rangle$	0.2387		
		$ H \rightarrow L + 3\rangle$	0.2174		

Table S6: The same information as in Table S2 but for the “6-X” hg-C₃N₄ QDs.

Structure	State	Configuration	Coefficient	E _x (eV)	<i>f</i>
6-Pris	7 ¹ A	$ H - 1 \rightarrow L\rangle$	0.3960	2.72 (455 nm)	0.02
		$ H - 3 \rightarrow L\rangle$	-0.3583		
		$ H - 2 \rightarrow L\rangle$	-0.3026		
6-CH ₃	13 ¹ A	$ H - 5 \rightarrow L + 2\rangle$	0.3067	3.82 (324 nm)	0.08
		$ H - 4 \rightarrow L + 1\rangle$	-0.2741		
		$ H - 5 \rightarrow L\rangle$	-0.2423		
6-CHO	12 ¹ A	$ H - 5 \rightarrow L + 1\rangle$	0.4625	3.76 (330 nm)	0.05
		$ H - 1 \rightarrow L + 1\rangle$	0.2697		
		$ H - 3 \rightarrow L + 1\rangle$	-0.2448		

6-COCH ₃	12 ¹ A	$ H - 5 \rightarrow L + 1\rangle$	0.3116	3.74 (331 nm)	0.06
		$ H - 1 \rightarrow L + 1\rangle$	0.4405		
		$ H - 8 \rightarrow L + 1\rangle$	0.1629		
6-COOH	12 ¹ A	$ H - 5 \rightarrow L + 1\rangle$	0.4481	3.70 (335 nm)	0.06
		$ H - 1 \rightarrow L + 1\rangle$	0.3037		
		$ H - 3 \rightarrow L + 1\rangle$	-0.2227		
6-OH	13 ¹ A	$ H - 1 \rightarrow L + 1\rangle$	0.3756	3.74 (332 nm)	0.14
		$ H - 1 \rightarrow L + 3\rangle$	-0.2859		
		$ H - 2 \rightarrow L + 2\rangle$	-0.2452		
6-F	12 ¹ A	$ H - 5 \rightarrow L + 1\rangle$	0.4108	3.72 (333 nm)	0.06
		$ H - 1 \rightarrow L + 1\rangle$	0.2965		
		$ H - 3 \rightarrow L + 1\rangle$	-0.2395		

Table S7: The oscillator strengths (f) and excitation energies (E_x) corresponding to the first excited state (1¹A) with the TD-DFT wave function dominated by the HOMO (H) \rightarrow LUMO (L) excitation.

Structure	E_x (eV)	f
1-Pris	4.06	0.0000
1-CH ₃	4.09	0.0003
1-CHO	3.79	0.0097
1-COCH ₃	3.83	0.0079
1-COOH	3.85	0.0066
1-OH	4.07	0.0055
1-F	4.07	0.0045
3-Pris	3.26	0.0005
3-CH ₃	3.24	0.0004
3-CHO	3.16	0.0011
3-COCH ₃	3.18	0.0013
3-COOH	3.18	0.0015
3-OH	3.23	0.0007
3-F	3.20	0.0014
4-Pris	3.14	0.0032
4-CH ₃	3.15	0.0031
4-CHO	3.10	0.0000
4-COCH ₃	3.11	0.0002
4-COOH	3.11	0.0003
4-OH	3.15	0.0020
4-F	3.12	0.0003
5-Pris	2.95	0.0007
5-CH ₃	2.94	0.0006
5-CHO	2.95	0.0009
5-COCH ₃	2.95	0.0008
5-COOH	2.95	0.0009

5-OH	2.95	0.0007
5-F	2.95	0.0010
6-Pris	2.03	0.0003
6-CH ₃	3.07	0.0037
6-CHO	3.06	0.0022
6-COCH ₃	3.06	0.0026
6-COOH	3.06	0.0025
6-OH	3.07	0.0034
6-F	3.06	0.0025

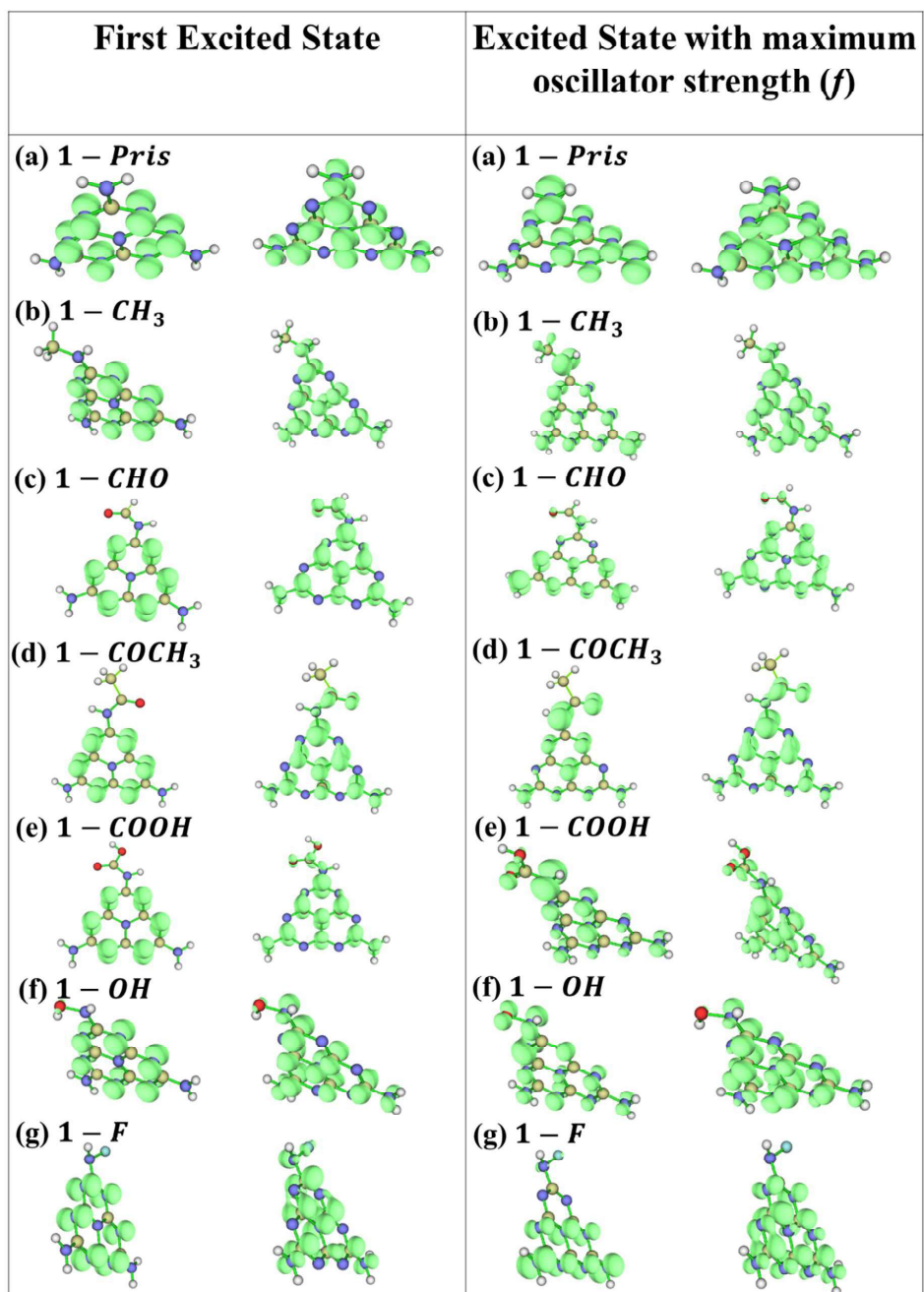


Figure S8: Spatial distribution (shown in green) of the photo-induced electrons (right) and holes (left) at the first excited state and the excited state with maximum oscillator strength for the 1-X structures. Here yellow, blue, grey, red, and cyan spheres represent the carbon, nitrogen, hydrogen, oxygen, and fluorine atoms, respectively.

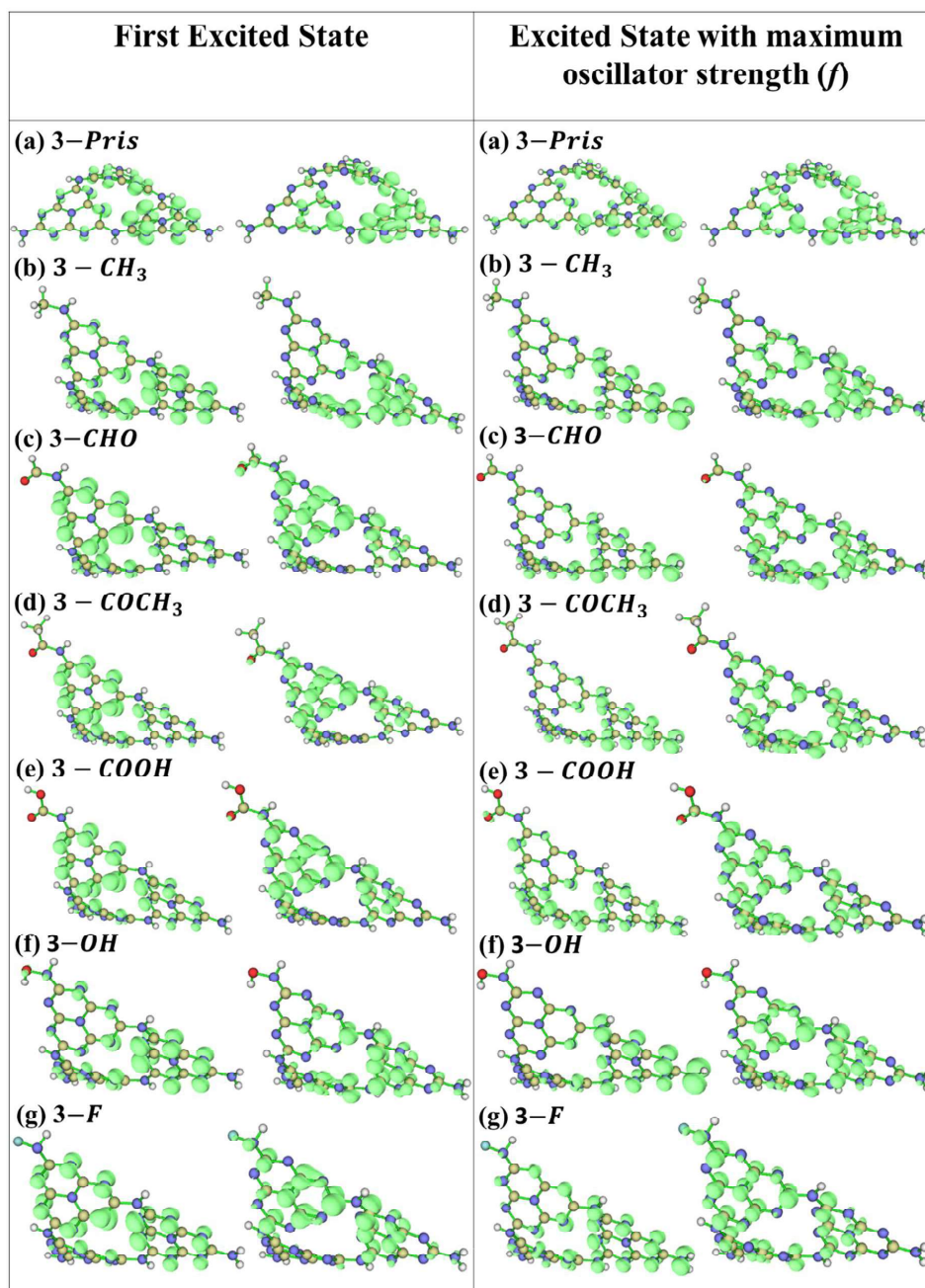


Figure S9: Spatial distribution (shown in green) of the photo-induced electrons (right) and holes (left) at the first excited state and the excited state with maximum oscillator strength for the 3-X structures. Here yellow, blue, grey, red, and cyan spheres represent the carbon, nitrogen, hydrogen, oxygen, and fluorine atoms, respectively.

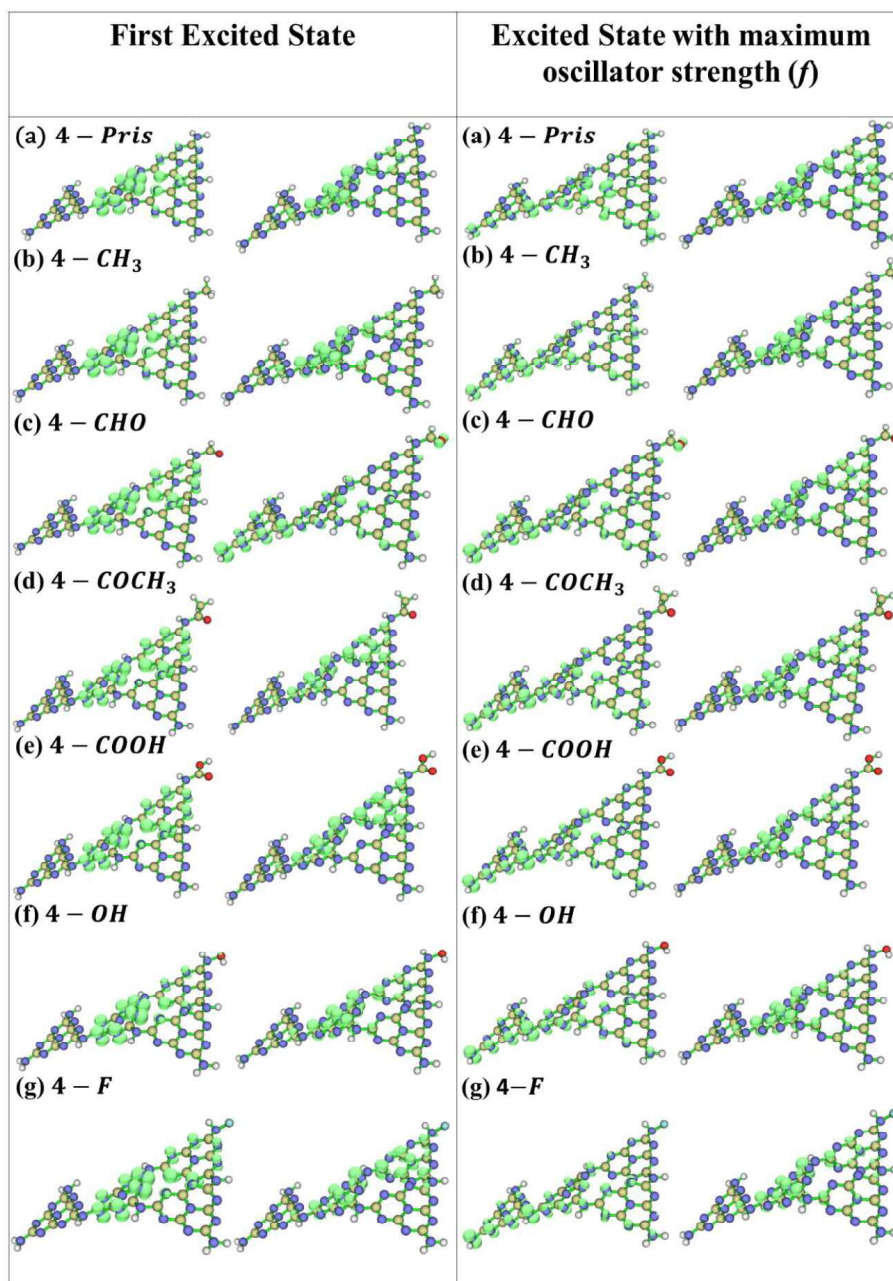


Figure S10: Spatial distribution (shown in green) of the photo-induced electrons (right) and holes (left) at the first excited state and the excited state with maximum oscillator strength for the 4-X structures. Here yellow, blue, grey, red, and cyan spheres represent the carbon, nitrogen, hydrogen, oxygen, and fluorine atoms, respectively.

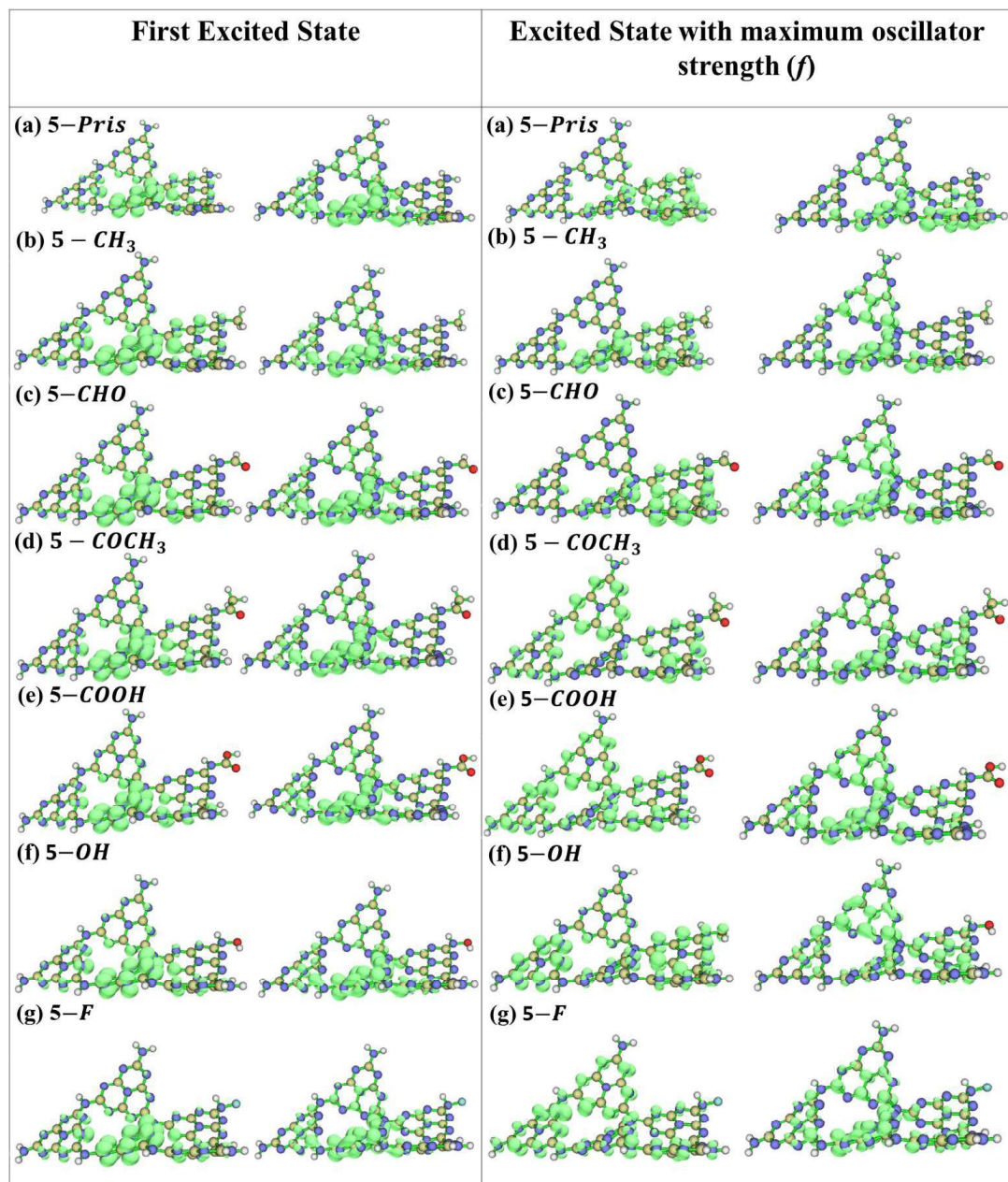


Figure S11: Spatial distribution (shown in green) of the photo-induced electrons (right) and holes (left) at the first excited state and the excited state with maximum oscillator strength for the 5-X structures. Here yellow, blue, grey, red, and cyan spheres represent the carbon, nitrogen, hydrogen, oxygen, and fluorine atoms, respectively.

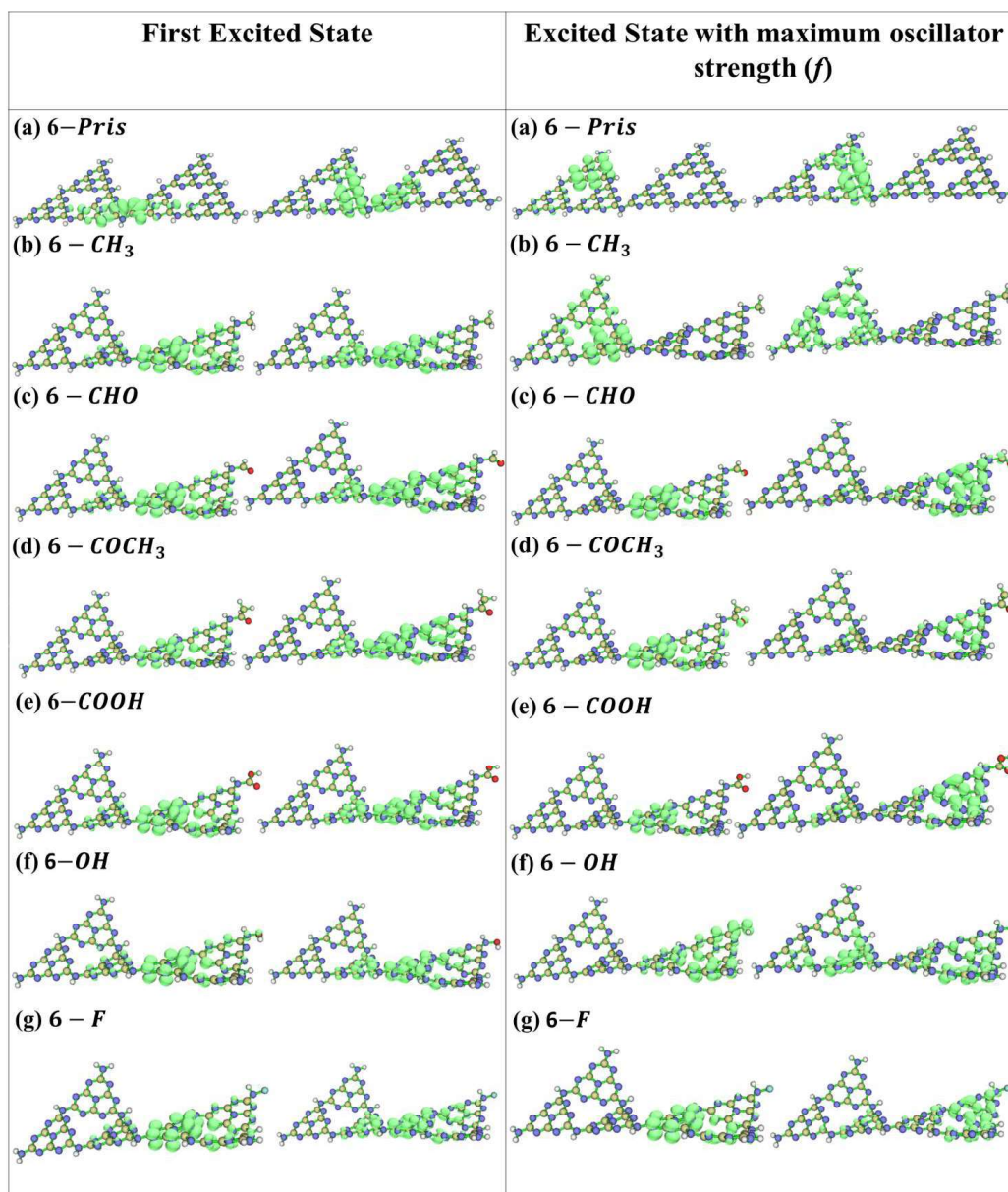


Figure S12: Spatial distribution (shown in green) of the photo-induced electrons (right) and holes (left) at the first excited state and the excited state with maximum oscillator strength for the 6-X structures. Here golden, blue, grey, red, and cyan spheres represent the carbon, nitrogen, hydrogen, oxygen, and fluorine atoms, respectively.